Author/s:
Jung, YJ;Almasi, A;Sun, S;Yunzab, M;Baquier, SH;Renfree, M;Meffin, H;Ibbotson, MR

Title:
Feature selectivity and invariance in marsupial primary visual cortex

Date:
2025-01-15

Citation:
Jung, Y. J., Almasi, A., Sun, S., Yunzab, M., Baquier, S. H., Renfree, M., Meffin, H. & Ibbotson, M. R. (2025). Feature selectivity and invariance in marsupial primary visual cortex. Journal of Physiology, 603 (2), pp.423-445. https://doi.org/10.1113/JP285757.

Persistent Link:
https://hdl.handle.net/11343/359395

The Journal of Physiology

Feature selectivity and invariance in marsupial primary visual cortex

Young Jun Jung[1,2,3], Ali Almasi[2], Shi Sun[2], Molis Yunzab[2], Sebastien H. Baquier[4], Marilyn Renfree[5], Hamish Meffin[1] and Michael R. Ibbotson[1,2,3]

[1]*Department of Biomedical Engineering, The University of Melbourne, Melbourne, Victoria, Australia*
[2]*National Vision Research Institute, Melbourne, Australian College of Optometry, Victoria, Australia*
[3]*Department of Optometry and Vision Sciences, The University of Melbourne, Melbourne, Victoria, Australia*
[4]*Melbourne Veterinary School, Faculty of Science, The University of Melbourne, Melbourne, Victoria, Australia*
[5]*School of BioSciences, The University of Melbourne, Melbourne, Victoria, Australia*

Handling Editors: David Wyllie & Jing-Ning Zhu

The peer review history is available in the Supporting Information section of this article (https://doi.org/10.1113/JP285757#support-information-section).

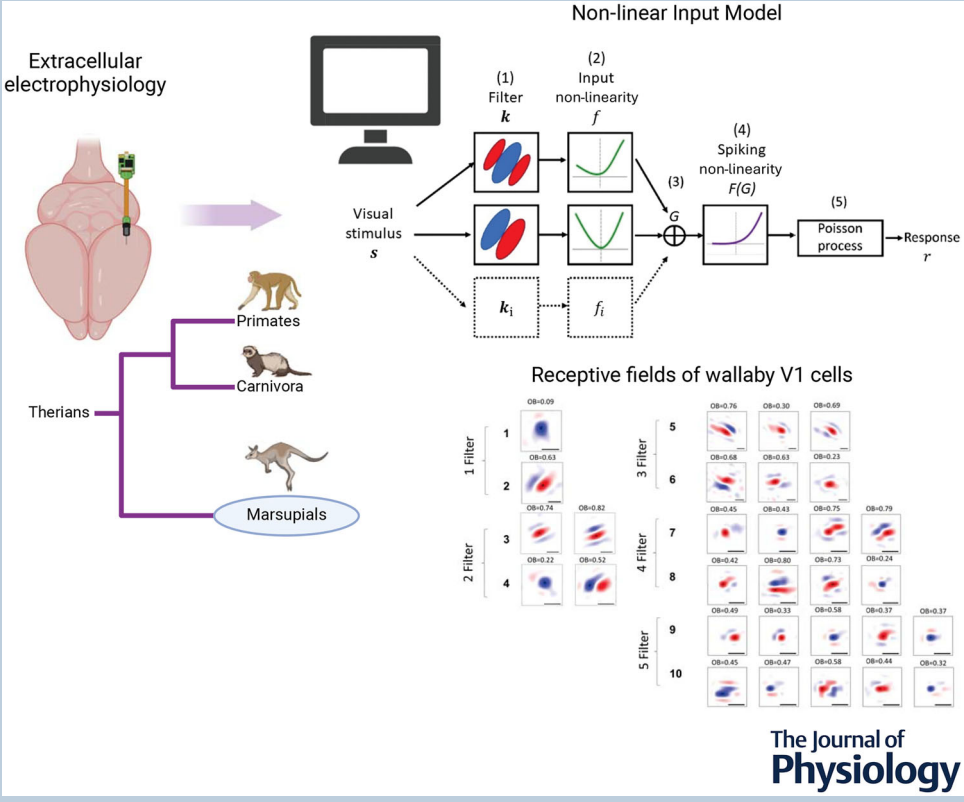

Abstract figure legend The primary visual cortex (V1) in mammals is essential for processing complex visual stimuli, with neurons exhibiting selectivity for edge orientation and position. Extracellular recordings and non-linear input model analysis were used to recover spatial receptive fields and to compare visual processing mechanisms in marsupials with those in eutherian mammals.

H. Meffin and M. R. Ibbotson contributed equally to this work.

DOI: 10.1113/JP285757

Abstract A fundamental question in sensory neuroscience revolves around how neurons represent complex visual stimuli. In mammalian primary visual cortex (V1), neurons decode intricate visual features to identify objects, with most being selective for edge orientation, but with half of those also developing invariance to edge position within their receptive fields. Position invariance allows cells to continue to code an edge even when it moves around. Combining feature selectivity and invariance is integral to successful object recognition. Considering the marsupial–eutherian divergence 160 million years ago, we explored whether feature selectivity and invariance was similar in marsupials and eutherians. We recovered the spatial filters and non-linear processing characteristics of the receptive fields of neurons in wallaby V1 and compared them with previous results from cat cortex. We stimulated the neurons in V1 with white Gaussian noise and analysed responses using the non-linear input model. Wallabies exhibit the same high percentage of orientation selective neurons as cats. However, in wallabies we observed a notably higher prevalence of neurons with three or more filters compared to cats. We show that having three or more filters substantially increases phase invariance in the V1s of both species, but that wallaby V1 accentuates this feature, suggesting that the species condenses more processing into the earliest cortical stage. These findings suggest that evolution has led to more than one solution to the problem of creating complex visual processing strategies.

(Received 3 October 2023; accepted after revision 15 November 2024; first published online 3 December 2024)
Corresponding author Y. J. Jung: Department of Biomedical Engineering, The University of Melbourne, Melbourne, VIC, Australia. Email: jason.jung@unimelb.edu.au

Key points

- Previous studies have shown that the primary visual cortex (V1) in mammals is essential for processing complex visual stimuli, with neurons displaying selectivity for edge orientation and position.
- This research explores whether the visual processing mechanisms in marsupials, such as wallabies, are similar to those in eutherian mammals (e.g. cats).
- The study found that wallabies have a higher prevalence of neurons with multiple spatial filters in V1, indicating more complex visual processing.
- Using a non-linear input model, we demonstrated that neurons with three or more filters increase phase invariance.
- These findings suggest that marsupials and eutherian mammals have evolved similar strategies for visual processing, but marsupials have condensed more capacity to build phase invariance into the first step in the cortical pathway.

Introduction

Visual processing occurs in a hierarchical manner, with increasingly complex and abstract features being extracted as signals progress through multiple neural processing steps, from detecting light in single photoreceptor cells to recognizing complex objects such as faces (Almasi et al., 2020; Felleman & Van Essen, 1991; Kendrick et al.,

Young Jun Jung is a neuroscientist trained at the University of Melbourne. He holds a Lions Vision Research Fellowship under the supervision of Professor Michael Ibbotson at the Department of Biomedical Engineering, University of Melbourne. This prestigious, internationally recognized fellowship is designed to train the next generation of leaders developing novel medical technologies for visual disease treatment. Prior to this fellowship, he completed his PhD (2021) in vision science from the Department of Optometry and Vision Sciences at the University of Melbourne. His current postdoctoral work aims to understand how neural information is processed in the brain.

1996; Riesenhuber & Poggio, 1999). When Hubel & Wiesel (1959, 1962) first measured the receptive fields (RFs) of cells in cat primary visual cortex (V1), they found that most cells preferentially responded to edges of a particular orientation, termed 'orientation selectivity'. As such, V1 appeared to be the first place where the advanced components of features in the visual image were extracted. Amongst the orientation selective cells, they further distinguished two cell types: simple and complex. For simple cells, the image disturbances that created the edge needed to have a particular orientation and location on the retina, invaluable for determining where the edge is in a retinocentric fashion (Kravitz et al., 2013). Conversely, complex cells were equally selective for orientation, but they were invariant to edge locations within their RFs, thus enabling the detection of edges regardless of retinal location. The capacity for selectivity and invariance in the same neural network is an essential characteristic for advanced object recognition (Almasi et al., 2020).

To date, the great majority of studies on V1 have been conducted on a small subset of extant eutherian mammals, such as primates, cats, ferrets and rodents (Fig. 1). This leaves open many questions about the evolution of the primary visual cortex. In mammalian evolution, the two largest infraclasses, eutheria and metatheria (marsupials), diverged from the progeniture therians about 160 million years ago (Luo et al., 2011) (Fig. 1). Given that the marsupials represent a phylogenetically distinct infraclass of mammals that arose directly from the therians, rather than as a sub-branch of the eutherian radiation, it is interesting to understand if mechanisms for visual processing evolved in a similar manner to those in eutherians (Jung et al., 2022; Jung et al., 2023).

It is more common for brain evolution to be discussed in the context of anatomical adaptations (e.g. whisker barrels and brain casts) (Azevedo et al., 2009; Inan & Crair, 2007), but we consider it equally important to search for mechanistic adaptations in brain functions. For example, did the mechanisms for orientation selectivity and feature invariance evolve along the same lines in eutherians and marsupials? Gross anatomical studies certainly show that marsupials have an area that can be identified based on homology as V1 (Vidyasagar et al., 1992; Wimborne et al., 1999). Moreover, analysis using moving bars and gratings has shown that orientation selective cells exist in the V1s of three marsupials from two continents, the Australian possum (Crewther et al., 1984) and Tammar wallaby (Ibbotson & Mark, 2003) and the American opossum (Rocha-Miranda et al., 1976) (Fig. 1). Recent findings have also shown that the characteristic 'pinwheel' orientation

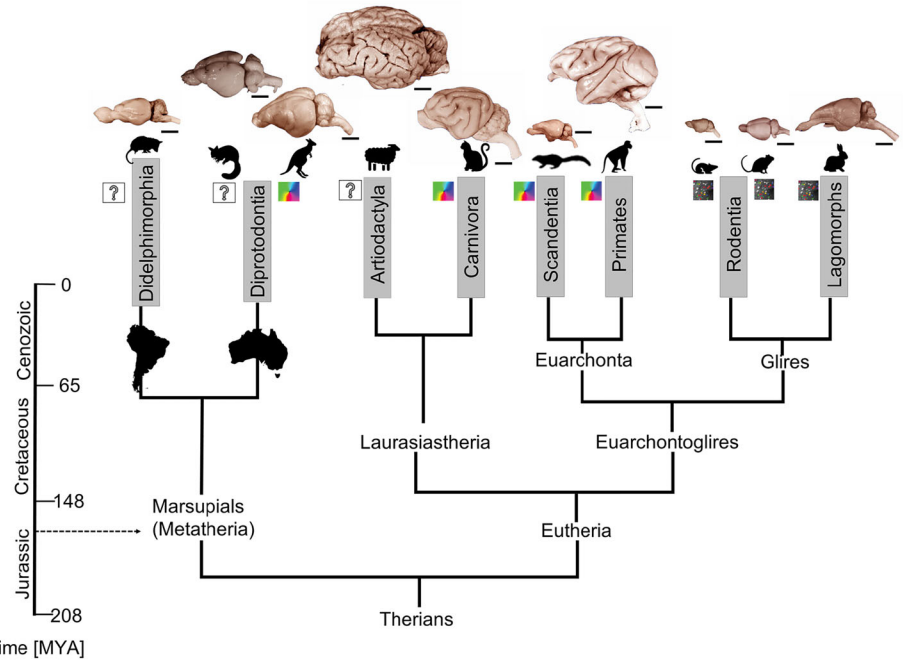

Figure 1. A simplified mammalian phylogenetic tree
The tree includes most of the species that have had their V1s studied using electrophysiology and (in some cases) imaging. MYA: millions of years ago. Images of brains are from the University of Wisconsin and Michigan State Comparative Mammalian Brain Collections (www.brainmuseum.org). If mammals in a particular phylogenetic line have pinwheel-like orientation preference maps, pinwheels are shown in small boxes; if they have salt-and-pepper maps, random dot patterns are shown; if imaging has not been conducted, a question mark is shown. From left to right, the species are: opossum, possum, wallaby, sheep, cat, tree shrew, macaque, mouse, rat and rabbit. [Colour figure can be viewed at wileyonlinelibrary.com]

preference maps found in primates, cats and ferrets (but not in rodents) are also found in wallaby (Jung et al., 2022) (Fig. 1).

The problem with most previous studies of V1 RFs, including those conducted on marsupials, is that the techniques used could only give a reasonable measure of each cell's RF if the summation properties were linear. As a result, for many years the mechanisms underlying non-linear complex cell behaviours were largely theoretical (Adelson & Bergen, 1985; Emerson et al., 1992). More recent analysis has assessed the stimulus response relationships of V1 cells using spike-triggered covariances, revealing the existence of multiple spatial filters (Liu et al., 2016; Nishimoto et al., 2006; Sharpee et al., 2006; Simoncelli et al., 2004; Touryan et al., 2005). Even more recently, tools from statistical inference have been used to fit parsimonious models of recorded neural responses to rich stimulus sets (Almasi et al., 2020; McFarland et al., 2013; Almasi et al., 2022). This type of analysis, exemplified by the non-linear input model (NIM) (Almasi et al., 2020; McFarland et al., 2013), is a data-driven approach in which the basic components are generic, mechanistic models that provide an approximation of neural processing without incorporating strong assumptions about the neuron's non-linear summation properties. As such, the models provide a useful tool when comparing RFs between species, as the possibility of introducing human bias is reduced.

Here we report the spatial RF characterization of V1 cells in a marsupial, an Australian wallaby, based on the application of the non-parametric NIM method and compare the data with that from the eutherian domestic cat (Almasi et al., 2020) (using the same stimuli and analysis). We find that general processing is similar but that neurons with two spatial filters in wallaby V1 have a low percentage compared to cat, while those with three or more filters are far more common than in cat. This suggests that wallabies compress more feature invariance into the first stage of cortical processing than the cat. The results imply that there have been differences in the evolution of eutherian and marsupial visual cortex, even in species with similar sized brains and similar visual spatial resolution.

Materials and methods

Ethics approval and animals

Recordings were made from six male adult tammar wallabies (12–24 months), each weighing between 3.9 and 5.7 kg. The experiments were conducted using the facilities at the National Vision Research Institute (NVRI) and in accordance with the National Health and Medical Research Council's *Australian Code of Practice for the Care and Use of Animals for Scientific Purposes*. All experimental procedures were approved by the Animal Care Ethics Committee at the University of Melbourne (Approval ID: 1714178.1). Importantly, these experiments were conducted on the same six animals as used in a previously reported imaging study (Jung et al., 2022), thus conforming to the ethical requirement to use as few animals as possible.

Surgical procedures

The animals were fasted 1 day before the surgery, and only water was given. Lincomycin (10 mg/kg), spectinomycin (20 mg/kg) and paraffin oil (10 ml orally) were given to reduce intestinal bloating during prolonged anaesthesia. Ketamine (10 mg/kg), medetomidine (0.015 mg/kg) and methadone (0.4 mg/kg) were administered intramuscularly to induce anaesthesia. Phytomenadione (10 mg/kg) and tranexamic acid (100 mg/kg) were administered intramuscularly to prevent any bleeding. Animals were orotracheally intubated and maintained under anaesthesia with gaseous isofluorane (1–2%) in oxygen during surgery, and then transitioned to halothane (0.5%) mixed with a 2:1 mix of O_2 and N_2O during recordings. Craniotomy windows in the left hemisphere over V1 were exposed and the dura removed. Neuromuscular blockade was initiated and maintained with vecuronium bromide (0.05 mg/kg for induction and 0.1 mg/kg/h in 1 ml of Hartmann's solution containing 5% glucose for constant intravenous infusion) to eliminate eye movements. Throughout the anaesthesia, the animals received intravenous infusion containing Hartmann's solution (50% by volume) and 0.9% NaCl solution (50% by volume) at a rate of 2.5 ml/kg/h. Daily intramuscular injections of atropine (0.2 mg/kg), dexamethasone phosphate (1.5 mg/kg) and Clavulox (0.05 ml/kg) were administered to reduce salivation, prevent cerebral oedema and control infection, respectively. Atropine sulphate eye drops (1%) were administered daily to maintain pupil dilatations and prevent retraction of the nictitating membranes. Zero-power gaseous permeable contact lenses were used to protect the corneas. The refractive errors were measured using retinoscopy and corrected with spherical lenses placed in front of the eyes to have the stimulus focused on the retina. Animals were killed with an intravenous injection of an overdose of barbiturate (sodium pentobarbital; 150 mg/kg).

Visual stimuli

Visual stimuli were generated with a ViSaGe visual stimulus generator (Cambridge Research Systems, Cambridge, UK) and displayed on a calibrated, gamma-corrected LCD monitor (ASUS VG248QE,

1920 × 1080 pixels, refresh rate 60 Hz, 1 ms response time) at a viewing distance of 57 cm. White Gaussian noise (WGN) stimuli were used to estimate the spatial RFs of cortical cells. WGN images comprised 90 × 90 pixels over 30° of the visual field, with its mean pixel value matched to the mean luminance of the display monitor. Each noise block comprised 12,000 WGN images, which were each presented for 1/30 s. It was followed by a blank screen of the mean luminance, displayed for the same duration of 1/30 s. The blank screen was used to increase the overall response of the cell to the stimuli as it would minimize any temporal correlation in the responses. The standard deviation of each noise block was determined, to obtain 90% of individual pixels with non-saturated values between 0 and 1, while the remaining pixels were clipped to produce 10% saturation rate of the generated noise block. We also presented drifting sinusoidal gratings with a circular aperture (30° diameter) set to high contrast (Michelson contrast 100%) on a grey background at the mean luminance. We recorded from multiple cells simultaneously using 32-channel electrodes (see below). As wallaby cortex has orientation columns (Jung et al., 2022), most cells recorded from a given electrode had similar orientation tuning, but this was not always true. In preliminary recordings, we presented drifting gratings with various combinations of orientations, and spatial and temporal frequencies to determine the preferred orientation and general tuning properties of as many of the recorded cells on each multi-channel electrode as possible. For orientation, we used 16 drift directions equally spaced between 0° and 337.5°. Each stimulus direction was presented randomly for at least five trials. The process outlined here with drifting gratings was repeated again after the experiments with WGN to check that the optimum response parameters had not changed over time. In cases where an obvious change had occurred, the data were deemed to be compromised and not used for further analysis.

Data recording

Extracellular recordings were conducted using NeuroNexus 32-channel multi-electrode arrays (MEAs). We used two MEAs: a single shank probe (6 mm total length; 1 × 32 sites spaced at 100 µm intervals for the lower 3.2 mm) or a four-shank probe (6 mm total length; 4 × 8 sites spaced at 100 µm intervals for the lower 0.8 mm). The arrays were vertically inserted into the cortex using a piezoelectric drive (Burleigh inchworm and 6000 controller, Burleigh Instruments, Rochester, NY, USA). Extracellular signals from 32 channels were simultaneously acquired using a CerePlex acquisition system and Central software (Blackrock Microsystems, Salt Lake City, UT, USA) sampled at 30 kHz.

Spike-sorting

An automatic spike-sorting program called KiloSort (Pachitariu et al., 2016) was used to separate spikes from different neurons. The spike clusters were manually sorted for further verification using the graphical user interface phy (Rossant et al., 2016). Single units (SUs) were identified from the presence of well-separated clusters in their feature space and from the profound refractory period in their inter-spike interval histograms, which confirms that spikes are non-overlapping. For more detail refer to the methods in Jung et al. (2022).

Model estimation

We employed the NIM described by Almasi et al. (2020) to estimate the spatial RFs ($n = 195$). This framework is an adaptation of the original model introduced by McFarland et al. (2013) to estimate all model parameters simultaneously rather than sequentially for different parameter types. Figure 2 and the equation below describes the firing rate (r) of the cell as a function of the input visual stimulus ($\boldsymbol{s}$):

$$r = F\left(\sum_{i=1}^{m} f_i\left(\langle \boldsymbol{k}_i, \boldsymbol{s}\rangle\right)\right) \quad (1)$$

where $\boldsymbol{k}_i$ represents the parallel streams, $i = 1, \ldots, m$, of spatial filters used to process the stimulus ($\boldsymbol{s}$) and the feature contrast is defined as their inner product $c_i = \langle \boldsymbol{k}_i, \boldsymbol{s}\rangle$. The inputs from a number of parallel synaptic input streams (m) are summed to produce a generator signal $G = \sum_{i=1}^{m} f_i(\langle \boldsymbol{k}_i, \boldsymbol{s}\rangle)$. Each input is processed by an arbitrary input function $f_i(\cdot)$ of the feature-contrast (c_i), which models the spike rate inputs of presynaptic neurons to the recorded cell. The function $F(\cdot)$ is the spiking non-linearity that converts the generator signal G into firing rates (r). Spikes are then generated stochastically according to a Poisson process with rate r. The parameters in the NIM [i.e. filters $\boldsymbol{k}_i$, input non-linearity f_i and spiking non-linearity $F(\cdot)$] were estimated using the maximum log-likelihood method. The equation below describes the log-likelihood (LL) of the NIM model parameters in response to a visual stimulus:

$$LL\left(\boldsymbol{k}_i, f_i, F|\mathrm{R}_{\mathrm{obs}}, \boldsymbol{s}\right) = \sum_{t=1}^{N}\left[{\mathrm{R}_{\mathrm{obs}}}^{(t)} \log\left(r^{(t)}\right) - r^{(t)}\right] \quad (2)$$

where $t = 1, \ldots, N$ indexes mutually independent stimuli with measured (i.e. observed) responses $\mathrm{R}_{\mathrm{obs}} = \{r_{\mathrm{obs}}^{(1)}, \ldots, {r_{\mathrm{obs}}}^{(N)}\}$, i.e. spike counts, and the model-predicted response rate $r^{(t)}$. The model assumes that the responses $\mathrm{R}_{\mathrm{obs}} = \{r_{\mathrm{obs}}^{(1)}, \ldots, {r_{\mathrm{obs}}}^{(N)}\}$ (integer spike counts) are to mutually independent instances of

the stimuli $S = \{s^{(1)}, \ldots, s^{(N)}\}$ and adhere to a Poisson distribution function at each instance:

$$p\,(\mathrm{R_{obs}}|\mathrm{S}) = \frac{r^{\mathrm{R_{obs}}}\exp\,(-r)}{\mathrm{R_{obs}}!} \tag{3}$$

where r denotes the firing rate in response to the stimulus. The spike counts for each WGN stimulus were determined by pooling all the spikes observed after the stimulus presentation within a 1/30 s window shifted by the optimum latency. For each cell, the latency was manually optimized to maximize the mean response to WGN by finding the time when neurons start to spike after a stimulus presentation. In most cases, 30–40 ms was found to be the optimum latency.

Model representation

Spatial filters were represented as $\boldsymbol{k}_i\ (x, y) = \sum_{n,m=1}^{N} \xi_{knm}\Xi_{nm}(x, y)$ using a two-dimensional Fourier basis set of the form $\Xi_{nm}\ (x, y) = \aleph \sin(2\pi\, f_0(nx + my) + \varphi_{nm})$, where n and m are integers from the set $\{-N, -N+1, \ldots, N-1, N\}$, and φ_{nm} is a phase chosen to be either sine phase ($\varphi_{nm} = 0$ for $(m > 0)$) or $(m = 0\ \&\ n > 0))$ or cosine phase $(\varphi_{nm} = \pi/2$ for $(m < 0))$ or $(m = 0\ \&\ n \leq 0))$ (the conditions on n and m ensure there is no degeneracy in the basis). Here, (x, y) are the horizontal and vertical pixel locations, f_0 is the base spatial frequency and $\aleph$ is a normalization factor. We chose $N = 5$ to give $11 \times 11 = 121$ basis functions. This gave a representation of the spatial filter below a frequency of $N f_0$, which was calibrated to approximately match the upper cut-off spatial frequency of the cell (=10% of maximum amplitude), and covering 2.3 octaves to the lowest sampled spatial frequency (other than 0). A square spatial region of interest was selected to enclose each cell's RF filters spanning a single cycle of the lowest sampled frequency (i.e. of side $1/f_0$). This choice also resulted in the basis functions being orthonormal, which allowed straightforward computation of filter outputs from their coefficients, ξ_{knm}, by converting stimuli, such as WGN, into the Fourier basis representation. This representation was found to give superior fits compared to pixelized representations because it resulted in a dimensionality reduction that reduced the number of parameters in most cases and eliminated high-frequency noise from the fitting processes.

Input feature-contrast functions for each filter were represented as piecewise linear functions of the feature-contrast $f_k(\langle \boldsymbol{k_i}, \boldsymbol{s}\rangle) = \sum_{l=0}^{L} \beta_{kl}\Lambda_l(\langle \boldsymbol{k_i}, \boldsymbol{s}\rangle)$ using a set of tent basis functions of the form [2]:

$$\Lambda_l\ (c) = \left\{ \begin{array}{c} \frac{c-\bar{c}_{l-1}}{\bar{c}_l-\bar{c}_{l-1}} \text{if } c \in [\bar{c}_{l-1}, \bar{c}_l] \\ \frac{\bar{c}_{l+1}-c}{\bar{c}_{l+1}-\bar{c}_l} \text{ if } c \in [\bar{c}_l, \bar{c}_{l+1}] \\ 0 \text{ otherwise} \end{array} \right\}$$

with $L = 7$ equally spaced intervals $[\bar{c}_l, \bar{c}_{l+1}]$ chosen to cover the 2.5–97.5% interval in the distribution of feature contrast, c_k.

The output/spiking function, mapping generator potential to mean spike rate, was modelled as a log-exponential function $F(v) = \alpha\log[1 + \exp(\frac{v-\gamma}{\alpha})] + \delta$. This function transitions from a constant spontaneous spike rate of $\delta \geq 0$ when the generator potential is significantly below the threshold γ $(\frac{v-\gamma}{\alpha} \ll 0)$ to a linearly increasing function with unit gain when the generator potential is significantly above the threshold $(\frac{v-\gamma}{\alpha} \gg 0)$. The transition occurs over a range of spike rates determined by $\alpha > 0$ for which the function has a strictly convex shape.

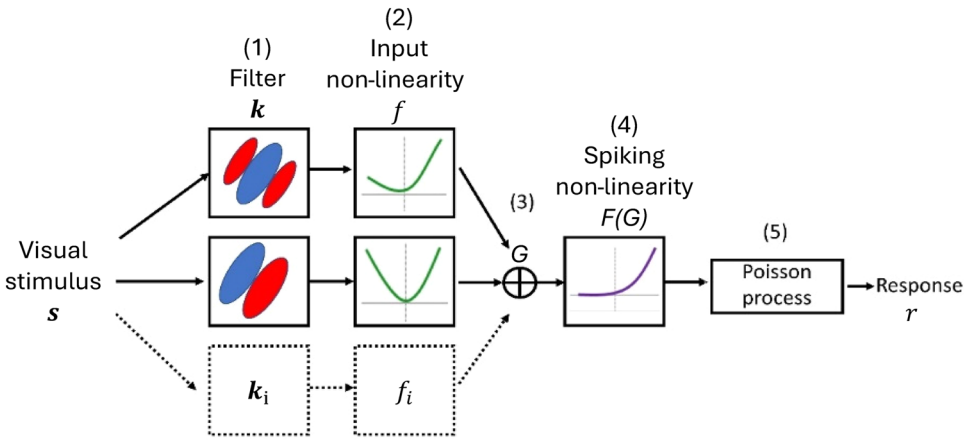

Figure 2. Schematic diagram of the NIM
In parallel streams: (1) visual stimulus is processed by several spatial filters, (2) the signal is then fed into the input non-linearity, (3) the parallel streams combine together to produce a generator signal, (4) the generator signal is processed by the spiking non-linearity and (5) the signal is randomized by a Poisson process to produce a spiking response for the neuron. [Colour figure can be viewed at wileyonlinelibrary.com]

Estimating global maxima

Due to the low dimensionality of this feature subspace, we performed a systematic brute-force search over parameter values that covered this space. In cases where cells were selective to more than one feature, filters were initialized as different linear combinations of the basis filters to cover the space approximately uniformly $\boldsymbol{k}_i^0 = \sum_{j=1}^{i} o_{ij}\ \boldsymbol{k}_j^{\mathrm{b}}$. The o_{kj} are parameters sampled from the upper hyper-sphere of dimension K, so as to preserve the unit norm of the initialized filters $\boldsymbol{k}_i^0$ given the normalized basis filters $\boldsymbol{k}_i^{\mathrm{b}}$ for the subspace; sampling only from the upper hypersphere avoids degenerating initializations that are simply opposite in sign to previous choices. For example, models with two filters are described by polar coordinates $o_{i1} = \cos\theta_i\,, \quad o_{i2} = \sin\theta_i$ with $\theta_i \in m\pi/M \| m = 0, \ldots, M-1$ & $\theta_2 > \theta_1$ (to avoid repeats or degeneracy). For higher dimensions, we used $o_{k1} = 1$ and $o_{kj} \in \{-1, +1\}$ to ensure sampling from the upper hyper-sphere in the K-dimensional feature space. For each set of initial filters, we ensured that they are independent but excluded the cases where the transformation was singular. For models with three filters this initialization yielded 16 different combinations of filter directions. For models with more than three filters, the number of all initial sets of filters grows combinatorially, which makes it computationally infeasible to probe them all. To deal with this, we randomly chose 30 initial sets for models with four filters, and 40 initial sets for models with five filters. All initial filters were normalized and for each initialized set of filters, a sequential optimization over input functions and the spike functions was performed to initialize these functions to their optimal values given the initial filters. Then a simultaneous optimization was performed over the subspace using the parameters ξ_{knm}, β_{kl} and (α, γ, δ) for the filters, input functions and spike function respectively. It should be noted in cases where models included only one spatial filter, the input function and the spike function can be composed together and be described by a function. Therefore, to avoid any degeneracy, for models with one spatial filter, the optimization was performed over the filter and input function parameters, while the spike function parameters were held fixed at $(\alpha, \gamma, \delta) = (1, 0, 0)$

Avoiding model degeneracy

The form of the NIM with a generator potential given as the sum of input feature-contrast functions is intended to approximate synaptic integration as a linear process given non-linear inputs from presynaptic neurons with different feature sensitivities. The form described here, with entirely arbitrary input functions, has the advantage that its representation is generally non-degenerate, meaning that there are no alternative parameter choices that can describe a functionally identical model. This is a consequence of the generator potential being an additively separable function of feature-contrast, and is true provided that four conditions are met for all values of i: i.e. (1) $\|\boldsymbol{k}_i\| = 1$, (2) $f_k\ (0) = 0$, (3) $f_k(c_{\max}) > f_k(c_{\min})$ and (4) $f_k^{''}(c) \neq 0$, where $c_{\max}$ and $c_{\min}$ are the maximum and minimum feature-contrast in the stimulus set, respectively. The first three conditions are arbitrary choices we implemented in the code to put the model in a standard form that would otherwise lead to degeneracy, while the final condition did not arise in our data set, but precludes models with purely linear or quadratic input functions: this latter situation admits a continuous family of linear transformations on the filters, leaving the overall model invariant. Note also that the choice of a single parameter, α, in two places in the spike function (multiplying the logarithm as well as in the denominator of the argument of the exponential), avoids a degeneracy with the overall scale of the input function through the parameters γ_{kl}.

Avoiding overfitting and determining the model hyperparameters

As the complexity (number of parameters) of a model increases, it becomes more susceptible to overfitting the data. Hence, it is crucial in model estimation to take necessary measures to prevent a model from overfitting. We employed cross-validation to determine the hyperparameters of the model. We determined the number of spatial filters within the RF of each cell using cross-validation. In doing so, the number of filters for each cell was systematically varied while the statistical significance of each filter was evaluated by bootstrapping. For this, we divided the data into a training set, which comprised four-fifths of the data, and a test set, which comprised the other one-fifth of the data. For each specified number of filters, we used the training set to estimate the filters, and then assessed the performance of the model by computing its log-likelihood using resampling from the test set (this was repeated 500 times). Thus, for each number of filters, we found a distribution for the log-likelihood computed on the test set. The inclusion of a new filter was counted as significant if it significantly improved the log-likelihood of the model on the test set (Z-score > 2). Regularization was also sought as another measure to prevent the input functions from overfitting to data. For this, we enforced regularization on the input functions by penalizing their second-order derivatives. The weight by which the regularization was added to the log-likelihood of the model (objective function) was determined using five-fold cross-validation, in the same process as described above.

Determining the number of filters

The number of spatial filters of each unit ($n = 195$) was systematically varied, and we evaluated the statistical significance of each filter using bootstrapping, which is a method commonly used in RF model evaluation (Almasi et al., 2020; Rust et al., 2005; Touryan et al., 2005) Four-fifths of the data were used to estimate the filters and the remaining one-fifth of the data was used as a test set. The performance of the models with different numbers of filters was evaluated by calculating the model log-likelihood derived from the resampling of the test set. This bootstrapping evaluation was repeated 500 times, and we calculated the distribution for the log-likelihood of each model with different numbers of filters. The optimal combination of filters was determined by first starting with the simplest combination of filters (one filter) and adding a new filter each time it significantly improved the log-likelihood of the model (i.e. Z-score > 2). Filters were added until there was no significant improvement in the log-likelihood.

To prevent the input functions from overfitting to the data, we used a similar cross-validation process as that described above. We applied regularization on the input functions by penalizing their second-order derivatives to get smooth functions. The penalization factor was determined using a cross-validation process, as described above. Four-fifths of the data were used to fit input functions using a combination of smoothing values and one-fifth of the data was used to assess the performance of the model by calculating the log-likelihood of the fitted models with different smoothing values. The procedure was repeated 500 times. The smoothing factor with the highest mean log-likelihood was determined for each cell.

Input non-linearity characterization

We characterized the model input function based on symmetry around the origin in feature-contrast. The symmetry index (SI) for each curve was calculated as:

$$SI\left[g\right] = \frac{\|g_e\|^2 - \|g_o\|^2}{\|g_e\|^2 + \|g_o\|^2} \tag{4}$$

where g_e and g_o represent the even and odd components of the function g, respectively:

$$g_e\ (x) = \frac{1}{2}\left(g\,(x) + g\,(-x)\right), \tag{5}$$

$$g_o\ (x) = \frac{1}{2}\left(g\,(x) - g\,(-x)\right) \tag{6}$$

The operator $\|\cdot\|$ represents the function norm in a Hilbert space, which is defined as:

$$\|g\,(x)\| = \sqrt{\int g^2\,(x)\,\mathrm{d}x} \tag{7}$$

The SI calculated varies from −1 (for an odd-symmetric function) to 1 (for an even-symmetric function). An SI of 0 represents a threshold-linear function (also known a rectified linear function).

Calculating modulation index from drifting gratings

For each single unit ($n = 195$), the relative modulation (F1/F0) ratio in response to optimal drifting sinusoidal gratings was calculated. In this case, optimal means the orientation, spatial frequency and temporal frequency that gave the largest spike rate for that cell in tests using drifting gratings. The amplitude of the Fourier coefficient at the fundamental frequency of the stimulus grating (F1) was divided by mean firing rate (F0), after subtracting the mean spontaneous activity from both measures (Crowder et al., 2008). The single unit was defined as a complex cell if its F1/F0 ratio was <1 and as a simple cell if its F1/F0 ratio was >1 (Skottun et al., 1991). Fourier coefficients were calculated by performing Fourier analysis on the spike train using the FFT function in MATLAB.

Calculating orientation selectivity (OS) from RF filters

For each single unit ($n = 195$), RF filters were transformed into the 2D Fourier spectrum, where the radial and angular coordinates of the Fourier domain represent the spatial frequency and orientation, respectively. Orientation tuning polar plots were obtained by sampling the Fourier amplitude spectrum at the preferred spatial frequency, which is the radial distance of the maximum of the amplitude spectrum. The OS of every unit was quantified with an orientation bias (OB) index as follows:

$$OB = \frac{\left|\sum_k R_k \exp\ (i2\theta_k)\right|}{\sum_k R_k} \tag{8}$$

where R_k represents the neuronal response at orientation θ_k, and $i = \sqrt{-1}$. We adopted this measure for the amplitude spectrum of filters. R_k represents the amplitude spectrum of the filter sampled at orientation θ_k.

An OB index of 0 indicates equal responses to all orientations, while an OB index of 1 indicates selectivity for only one orientation. Hence, orientation selectivity is greater as OB indices increase. For single units with more than one filter, the amplitude of the 2D Fourier spectrum for each filter was normalized and then averaged to obtain the OB.

Results

Here we define Area 17 as the primary visual cortex (V1) in both wallaby and cat. We recorded from 234 single units that were responsive to WGN in V1, from six

anaesthetized wallabies. Of these, we recovered the spatial RFs of 195 single units.

Spatial receptive fields in wallaby V1

The classification of RF types was based on the number of significant filters that were present in the estimated RF. Figure 3 shows 10 example units with all the RF filters characterized by the NIM. Units 1 and 2 are examples of RFs with one spatial filter. Unit 1 has a spatial filter that is tuned to blob-like features of the indicated brightness polarity. Using the OB index, we find that this unit is non-orientation selective (i.e. OB index $\leq$ 0.2). Unit 2 is selective for elongated Gabor-like features with alternate subfields of ON and OFF polarities and is highly orientation-selective (OB index > 0.6).

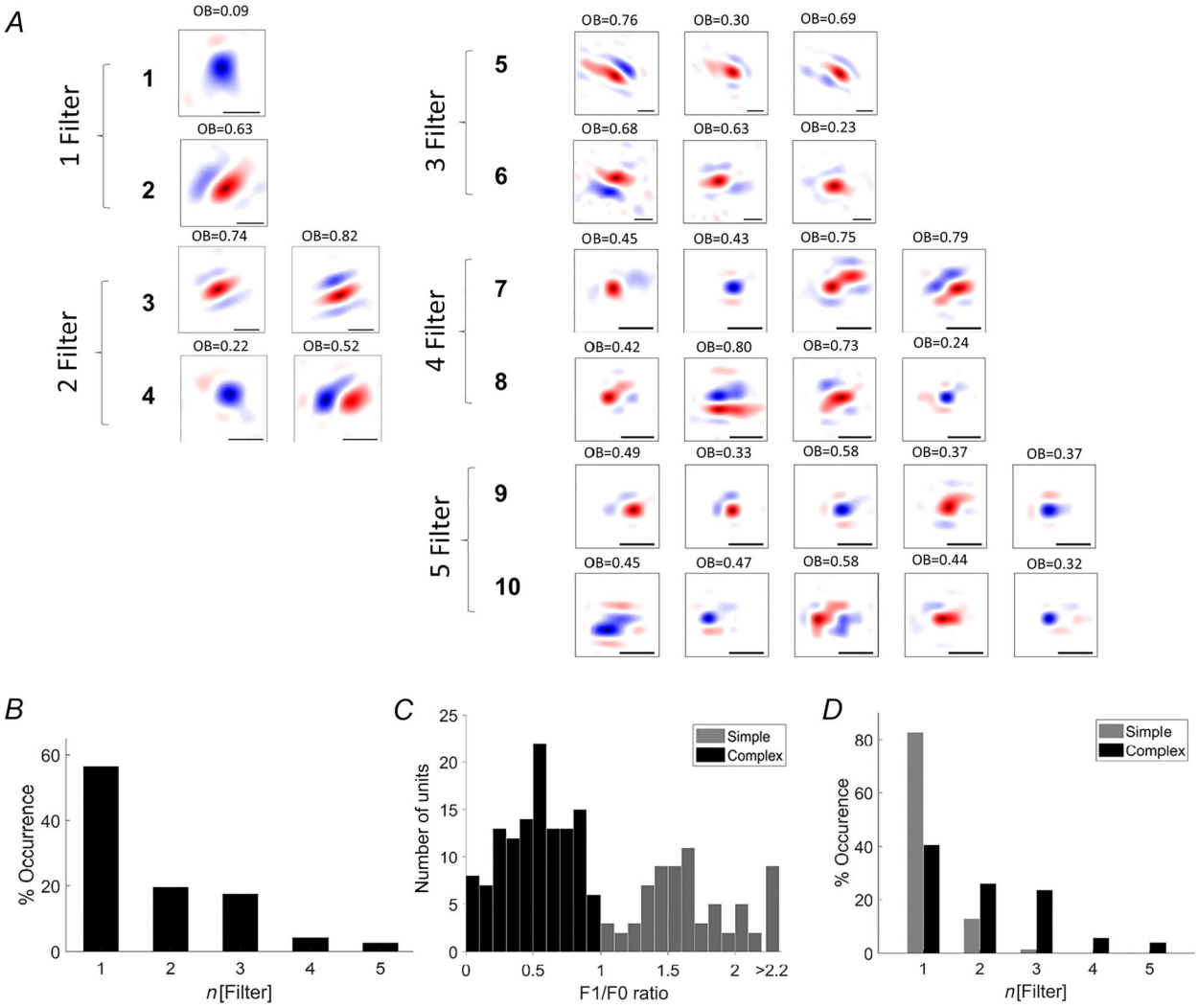

Figure 3. Spatial receptive fields in V1
A, 10 example units are presented in rows, labelled 1–10, and the filter types are laid out in columns, labelled Filters 1–5. The estimated RF filters are all spatially localized. Within the spatial RFs, red regions represent the ON-response subfields (i.e. responding to brightness increments) and blue regions represent the OFF-response subfields (i.e. responding to brightness decrements). The size of RFs is indicated by the scale bar, which represents 1° in visual space. OB = orientation bias. An OB index of 0 is a unit responding equally to all orientations, while an OB index of 1 is a unit responding only to a particular orientation. *B*, the distribution of single- and multi-filter units in the wallaby unit population. *C*, F1/F0 ratios for wallaby V1 units (n = 195). Grey and black columns represent simple and complex cells, respectively. The cells are binned into 0.1 bar widths. Cells with F1/F0 ratios > 2.2 are all presented to the far-right bar. The distribution of simple and complex cells was significantly different from unimodality (Hartigan's dip statistic: P = 0.03). *D*, bar graph showing the distribution of the number of RF filters obtained from the NIM for classical simple and complex cells. Note that many simple cells had only a single filter and many complex cells varied from one to five filters when assessed using the NIM. [Colour figure can be viewed at wileyonlinelibrary.com]

Table 1. Overall percentages of different filter types for wallabies and cats. Cat data from Almasi et al. (2020)

Species	One filter (%)	Two filters (%)	Three filters (%)	Four filters (%)	Five filters (%)
Wallaby	56	20	17	4	3
Cat	61	30	7	<1	<1

Units 3 and 4 are examples of RFs with two spatial filters. Unit 3 has spatial filters with the same orientation preferences, but the spatial phase is shifted by ∼90°, as expected from the energy model of spatial phase invariance (Adelson & Bergen, 1985; Emerson et al., 1992). The two filters in this unit are highly orientation selective (OB index > 0.7). Unit 4 has two spatial filters, with one filter selective for blob-like features and another selective for orientation with alternate subfields of ON and OFF polarities.

Units 5 and 6 are examples of RFs with three spatial filters. The three spatial filters of unit 5 are all orientation selective (OB index > 0.3) and share the same preferred orientation, but their phases are shifted by 120° across the different filters. Unit 6 is an example of RFs showing a mixture of filters responding to blob-like features and Gabor-like features, some only weakly orientation selective.

Units 7 and 8 are examples of RFs with four spatial filters. These units appear to mix filters that are highly orientation selective (e.g. OB index = 0.8) with those with weak orientation selectivity (e.g. OB index = 0.24). Units 9 and 10 are examples of RFs with five spatial filters. A common feature of the five-filter units was that the OB indices of all filters tended to be on the lower end of the scale, i.e. often 0.3–0.5 and always <0.6. Interestingly, 51% of the units with ≥3 filters had a mixture of filters that responded to blob-like and Gabor-like features.

Overall, the number of RF filters varied across the cell population, ranging from one to five. We report 56% of units (n = 110/195) with one filter, 20% (n = 39/195) with two filters, 17% with three filters (n = 33/195), 4% with four filters (n = 8/195) and 3% with five filters (n = 5/195) (Fig. 3*B*) (Table 1).

We also investigated the responses of our cells to drifting sinusoidal gratings. We classified simple and complex cells from our cell population based on their modulation ratio to drifting gratings (F1/F0 ratio). The F1/F0 ratios for the 195 units showed a clear bimodal distribution similar to that found previously (Ibbotson et al., 2005) (Fig. 3*C*), where the simple and complex cell populations were significantly different from unimodality (Hartigan's dip statistic: P = 0.03). Based on the separation line of F1/F0 = 1, we identified 41% as simple cells (n = 79/195) (grey bars) and 59% as complex cells (n = 116/195) (black bars). Figure 3*D* shows the distribution of the number of spatial filters identified using the NIM but using the grating data to divide the population into simple and complex cells. As expected from linear models, 84% of simple cells have one significant spatial filter. However, in the case of complex cells (black bar), a large portion differed from the expectation of the energy model (Emerson et al., 1992), with only 28% comprising two filters and the remaining 72% comprising either one filter (39%) or 3–5 filters (33%).

Orientation selectivity of V1 units

We revealed the structure of the spatial filters that make up V1 RFs and compared those physical structures with their OB index. RF filters were transformed into the 2D Fourier spectrum, where the radial and angular coordinates of the Fourier domain represent the spatial frequency and orientation, respectively. Orientation tuning polar plots were obtained by sampling the Fourier amplitude spectrum at the preferred spatial frequency, which is the radial distance of the maximum of the amplitude spectrum (described in Jung et al., 2022). We calculated an overall OB index for each unit by averaging the amplitude of the 2D Fourier spectrum for each unit's spatial filters (see Methods). Figure 4*A* presents the distribution of OS in OB indices of all the 195 units recorded. It is clear that units with elongated spatial filters have high OB indices and those with blob-like spatial filters are non-oriented (Fig. 4*B*). The great majority of cells (76%) were orientation selective (OB index > 0.2) and the percentage remains similar regardless of number of filters (77% for 1-filter units, 71% for 2-filter units, 77% for ≥3-filter units) (Fig. 4*C*). The mean OB indices for non-oriented cells were 0.11–0.13 for all numbers of filters. The mean OB indices were 0.39–0.44 for the orientation selective units. Interestingly, units with very high OB indices (>0.8) were absent in the ≥3-filter category but plentiful in the other two unit types.

Non-linear properties of V1 units

Neuronal response properties of different cell types are further examined by observing each cell's response profiles as functions of its RF feature-contrast. The feature-contrast for an RF filter is the inner product of the stimulus with the filter. It measures the contrast

level of the feature in the image that corresponds to the filter. Figure 5 shows the non-linearities plotted as input functions over the feature-contrast for three single units. Here, we have only shown the cell non-linearity prior to the application of the spiking non-linearity; the latter has a fixed parametric form of a log-exponential function similar to a soft thresholding function. The output of the input function is analogous to the sub-threshold membrane potential. The feature-contrast is presented in arbitrary units (a.u.) as it is normalized to the measured filter. The origin ($x = 0$ and $y = 0$) is indicated by the grey lines on the plot. The origin ($y = 0$) corresponds to the spontaneous level of activity. The SI, which describes the similarity between the positive and negative feature-contrasts of the curve, is indicated above the non-linearity plot.

A linear cell, typical of a simple cell, has opposite responses to opposite feature contrasts, resembling a monotonic function (odd symmetric; SI = −1). A linear filter could also respond to one feature-contrast, in which case its input function resembles a threshold-linear function (SI = 0). A non-linear filter, typical of a classical complex cell, responds equally to opposing feature-contrasts, resembling a squaring function (even symmetric; SI = 1). The top panel from Fig. 5*A* presents an example single unit with one spatial filter, which has an odd symmetric-input function (SI = −0.57), showing excitation to one polarity and inhibition to the opposite. The bottom panel from Fig. 5*A* presents an example unit with one spatial filter, which has an even-symmetric input function (SI = 0.96), responding almost equally to both polarities of the RF filter. Figure 5*B* shows an example unit with two spatial filters that have approximately even-symmetric input functions (SI = 0.79, SI = 0.95). The upper filter is biased towards stronger responses to ON stimuli, while the lower filter produces approximately equal responses to ON and OFF stimuli.

For multi-filter cells, the input functions were heavily biased toward even-symmetric functions (black bars in Fig. 5*C*), with 50% of filters showing SI > 0.75 and less than 10% of filters distributed towards odd-symmetric functions (SI > 0). For the single-filter cells, the distribution also peaked at even-symmetric input functions (white bars in Fig. 5*C*). The even-symmetric input functions for these single-filter cells show that they respond to both ON and OFF stimuli (example, Fig. 5*A*), which leads to non-linearities in their responses. However, the distribution across the SI was more even, with 29% of cells showing SI > 0.75 and 27% of filters distributed towards odd-symmetric functions (SI < 0). Moreover, we found that single-filter cells with a modulation index of F1/F0 < 1 (typical of a complex cell) were strongly biased

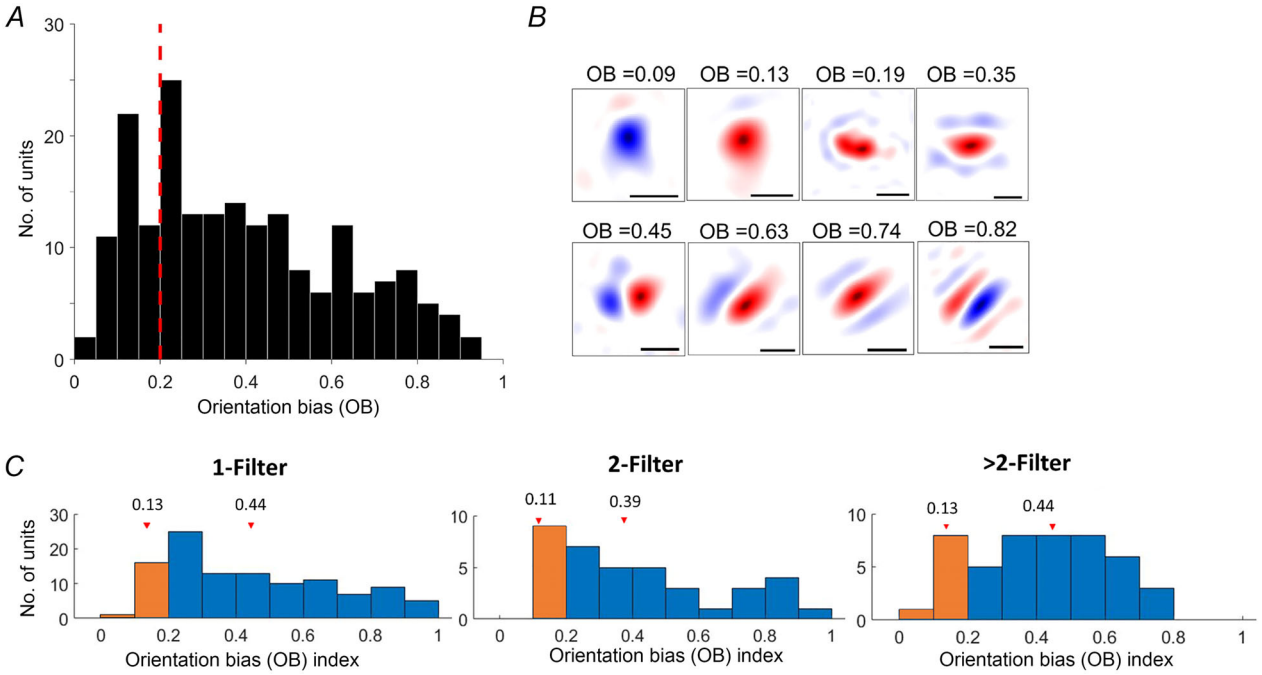

Figure 4. Orientation selectivity of V1 units
A, histogram showing the distribution of OB values of all 195 single units recorded. Red dashed line indicates the threshold (OB = 0.2) between non-oriented and oriented types. Of all the units recorded, 76% (n = 148/195) were oriented and 24% (n = 47/195) were non-oriented. *B*, example RFs of single-filter units with different OB values. *C*, histograms showing the OB indices for single-filter, double-filter and ≥3-filter units. Orange bars are non-oriented units; blue bars are orientation-selective units. Numbers with arrows above each plot show the mean non-oriented and oriented OB indices. [Colour figure can be viewed at wileyonlinelibrary.com]

towards even-symmetric functions (86% with SI > 0; grey bars in Fig. 5*D*). We also found that multi-filter cells with a modulation index of F1/F0 < 1 were even more strongly biased towards even-symmetric functions (96% with SI > 0; black bars in Fig. 5*D*).

Overall response selectivity and invariance

The selectivity or invariance of a cell to image features is contingent upon the spatial configuration of its filters, the relationship between these filters, and the characteristics of the input functions (non-linearities). Figure 6 presents

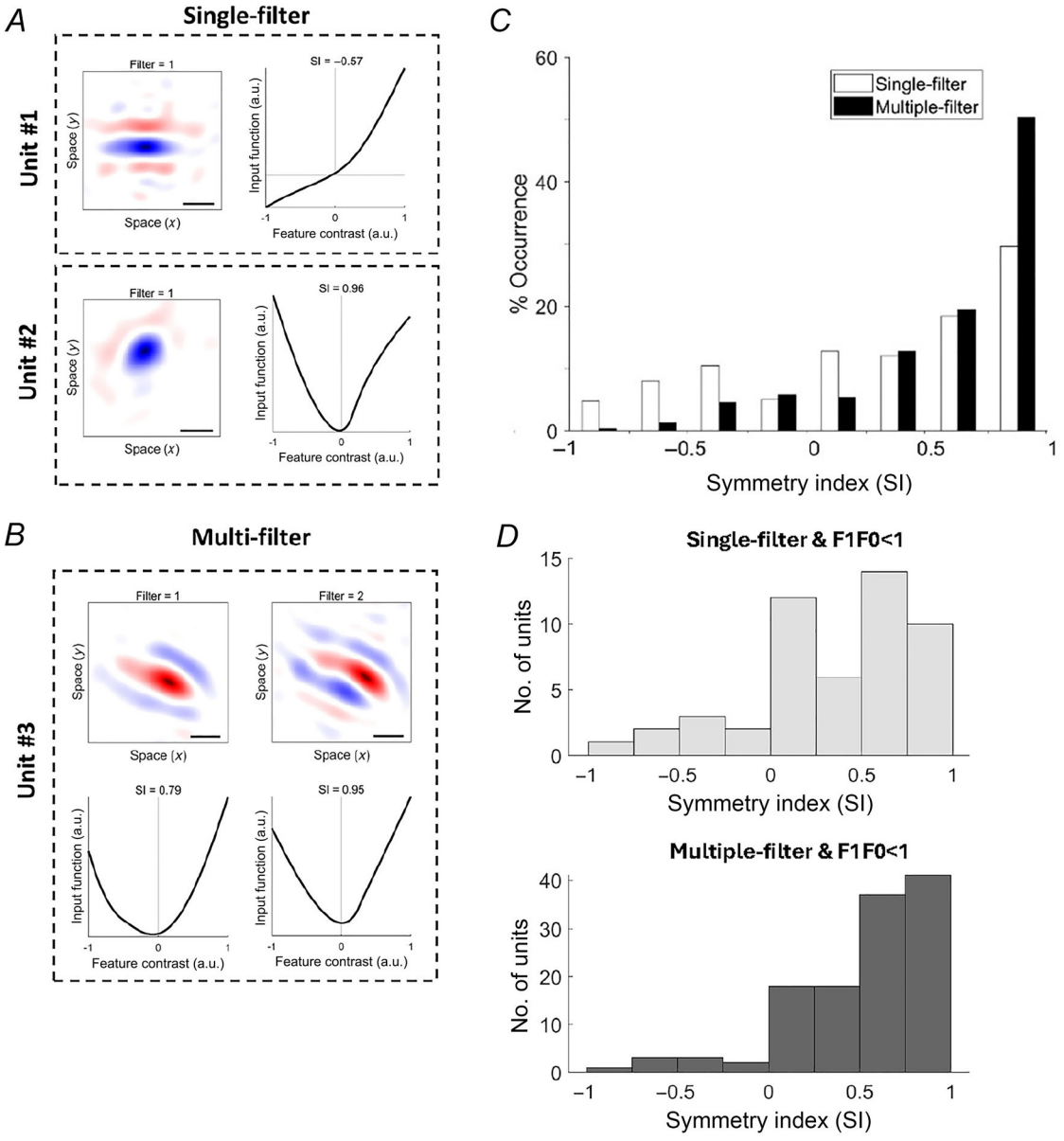

Figure 5. Non-linear properties of V1 units
Three example units with their RFs and corresponding input functions from the NIM. The red regions are ON responses and blue regions are OFF responses, in *x* and *y* space. The black bar indicates 1° in visual space. On the right side of the filters are the respective input non-linearities plotted as input functions over feature contrast (arbitrary units: a.u.), and the grey lines represent the origin ($x = 0$, $y = 0$). The titles for the input function plots show the symmetry index (SI). *A*, top panel: single-filter unit with an odd symmetric input function (SI = −0.57). Bottom panel: single-filter unit with an even symmetric input function (SI = 0.96). *B*, multi-filter unit with two spatial filters that have approximately even-symmetric input functions (SI = 0.79, SI = 0.95). *C*, distributions of the SI of identified input functions for single-filter (white bars) and multi-filter cells (black bars). *D*, distribution of the SI values of identified input functions for single-filter and multi-filter cells with F1/F0 ratio < 1 (classically defined as complex cells). [Colour figure can be viewed at wileyonlinelibrary.com]

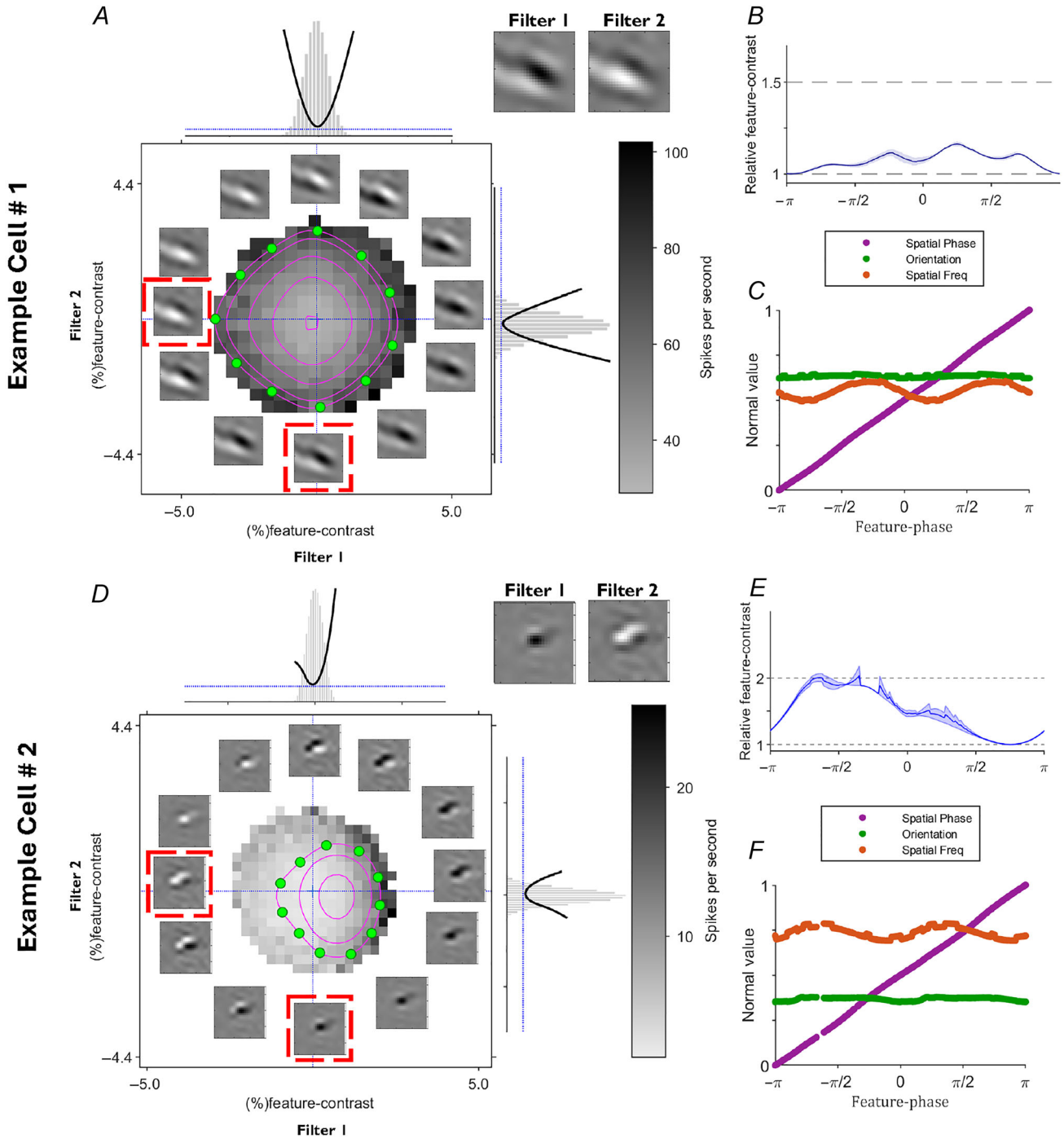

Figure 6. Selectivity and invariance in wallaby V1 cell
A, an example model fit #1 for a cell with spatial phase invariance (for the example 1 cell, the estimated input non-linearities for both filters are close to quadratic). For this cell, the spectrum of interpolated features producing equal responses spans 2π radians of feature-phase due to the closed elliptical isoresponse contours. The example cell is invariant to spatial phase because it responds equally to interpolated features that are spanning the full 360° of spatial phase. *B*, an example model fit #2 for a cell with two not even-symmetric input functions. As a result of the openness of the isoresponse contours for this cell, the relative feature-contrast varies significantly. For each example, two spatial RF filters (Filter 1 and Filter 2), derived from a WGN stimulus region, are shown on the top right. The two-dimensional feature subspace plot shows the mean spike rates, represented by various shades of grey, in response to each interpolated feature embedded in WGN. Magenta isoresponse contours indicate equal spike rates for various feature-phases and contrasts. Green dots represent a selection of interpolated features, each associated with specific coordinates within the feature subspace. Non-linearities for these filters are represented

by black curves over grey bar-graphs, depicting cell responses across the WGN stimuli in feature space. *B* and *E*, feature-contrast of interpolated features along isoresponse contours is plotted against feature-phase, averaged across different spike rates. *C* and *F*, the features interpolated (i.e. orientation, spatial frequency, spatial phase) at different feature-phases are sampled from an isoresponse contour within the cell's feature spectrum. The degree of variation observed in each feature characteristic is normalized relative to its inherent range of variation. [Colour figure can be viewed at wileyonlinelibrary.com]

the estimated RF filters for a cortical cell corresponding to its primary visual features. The mean spike rates are represented by various shades of grey, in response to each interpolated feature within the feature subspace. This two-dimensional subspace is characterized by the feature-contrast associated with each primary feature embedded in WGN. The feature-contrast equates to the output produced by the corresponding (normalized) filter. The magenta curves in the plot denote iso-response contours for multiple response levels. Adjacent to each axis in the subspace plot, we provide the fitted input function (depicted as black lines) and present the distribution of feature-contrast in the WGN stimuli, visualized as grey histograms.

For the cell featured in Figure 6, the estimated input non-linearities for both filters closely approximate quadratic functions (see grey histograms). We present a selection of interpolated features, each associated with specific coordinates within the feature subspace, indicated by green dots. The angular position of each green dot in relation to the x-axis is denoted as the feature-phase of the corresponding feature. This feature-phase serves as a unique identifier for the spatial configuration of the feature, independent of its contrast. The comprehensive space encompassing all spatial feature configurations, irrespective of contrast, is formally termed the feature spectrum.

It is essential to emphasize that the range of interpolated characteristics that produce equivalent responses extends across 2π radians of the feature-phase. This invariance to feature-phase remains robust regardless of the specific isoresponse contour chosen. When we standardize each contour relative to its minimum feature-contrast (which corresponds to the radial distance in the feature subspace), the contours exhibit minimal variation (as depicted in Fig. 7*B*). Consequently, the functional relationship between relative feature-contrast and feature-phase remains unaffected by fluctuations in spike rate.

The collection of interpolated features that elicit identical spike rates in the feature subspace shows the cell's selectivity or invariance to various feature attributes. We characterized these interpolated features within the subspace based on their peak orientation, peak spatial frequency and relative spatial phase. In the case of the sample cell, it demonstrates invariance to spatial phase because it responds equally to interpolated features spanning the entire 360° range of spatial phase (illustrated by the thick magenta line in Fig. 6*C*). Conversely, when it comes to orientation and spatial frequency, the interpolated features on the isoresponse contour cover only a small portion of the potential range (as shown by the thick green and orange lines in Fig. 6*C*). Consequently, this cell exhibits selectivity for orientation and spatial frequency but largely remains invariant to spatial phase and brightness polarity. We also encountered many two-filter cells whose isoresponse contours in their feature subspace were not elliptical (Fig. 6*D*). For these cells the relative feature-contrast varies significantly because their isoresponse contours were open. They passed through only part of the circle of feature-phase, independent of the spike rate.

We examined the tuning breadths calculated from multi-filter cells and observed the theoretical tuning breadths that would result if the cells had access solely to linear or quadratic-like input functions. Figure 7 shows the variability in tuning widths concerning orientation, spatial frequency and spatial phase across a population of cells with two or more filters ($n = 100$). The left column depicts cells with two filters, the middle column three filters, and the right column cells with four and five filters. The grey triangular symbols positioned above the bar graphs highlight cells ($n = 14$) that exhibited blob-like RFs. In these histograms, the thick bars represent the tuning breadths acquired from the cells. The thin black bars represent the tuning breadths if the cell spectrum is sampled using a combination of quadratic-like input functions. Conversely, the thin white bars represent the tuning width of the linear model, aligned to the interpolated feature to which the cell responds at minimum feature-contrast. These values establish upper and lower bounds for the cell's tuning breadth, respectively, as they correspond to the maximum and minimum feature-phase bandwidths. For most cells with two filters, they displayed a high degree of selectivity for feature orientation (90% exhibited orientation breadths $< 45°$; thick bars, Fig. 7*A*). However, the subpopulation of cells with three filters demonstrated invariance to larger deviations in orientation (76% had breadths $> 45°$; Fig. 6*A*). Cells with four and five filters showed invariance to the widest deviation of orientations, with all showing tuning breadths $>120°$ (Fig. 7*A*). Many cells with three or more filters sampled a broader range of orientations than expected from the linear model, offering significantly greater orientation invariance (thick black bars compared to thin white bars with grey triangles above, Fig. 7*A*).

For most multi-feature cells, they displayed a low degree of selectivity for spatial frequency (65% had tuning width >0.1 cycles per degree (cpd), maximum 0.5 cpd).

Furthermore, most cells had spatial frequency tuning breadths similar or equal to the maximum allowed by the model with quadratic-like input functions, as indicated by the thin black bars rarely surpassing the thick black bars (Fig. 7*B*). Cells with three or more filters exhibited the greatest spatial frequency tuning breadths (Fig. 7*B*). Some of these cells also expanded their spatial frequency tuning breadths to some extent due to the non-linear sampling of their response functions, as evidenced by the thick black bars being taller than the thin white bars (Fig. 7*B*).

The most significant results were obtained when assessing the invariance to spatial phase. In the entire population of cells with two filters, only 4% had spatial phase tuning breadths that covered 360° (thick bars, Fig. 7*C*). For comparison, in the cat V1 cell population, 12% had spatial phase tuning breadths that covered 360° (Fig. 7*D*). For the wallaby V1 cell population, 49% of the subpopulation with three filters had spatial phase tuning breadths that covered 360° (Fig. 7*C*). For wallaby cells with four and five filters, 75% had spatial phase tuning breadths

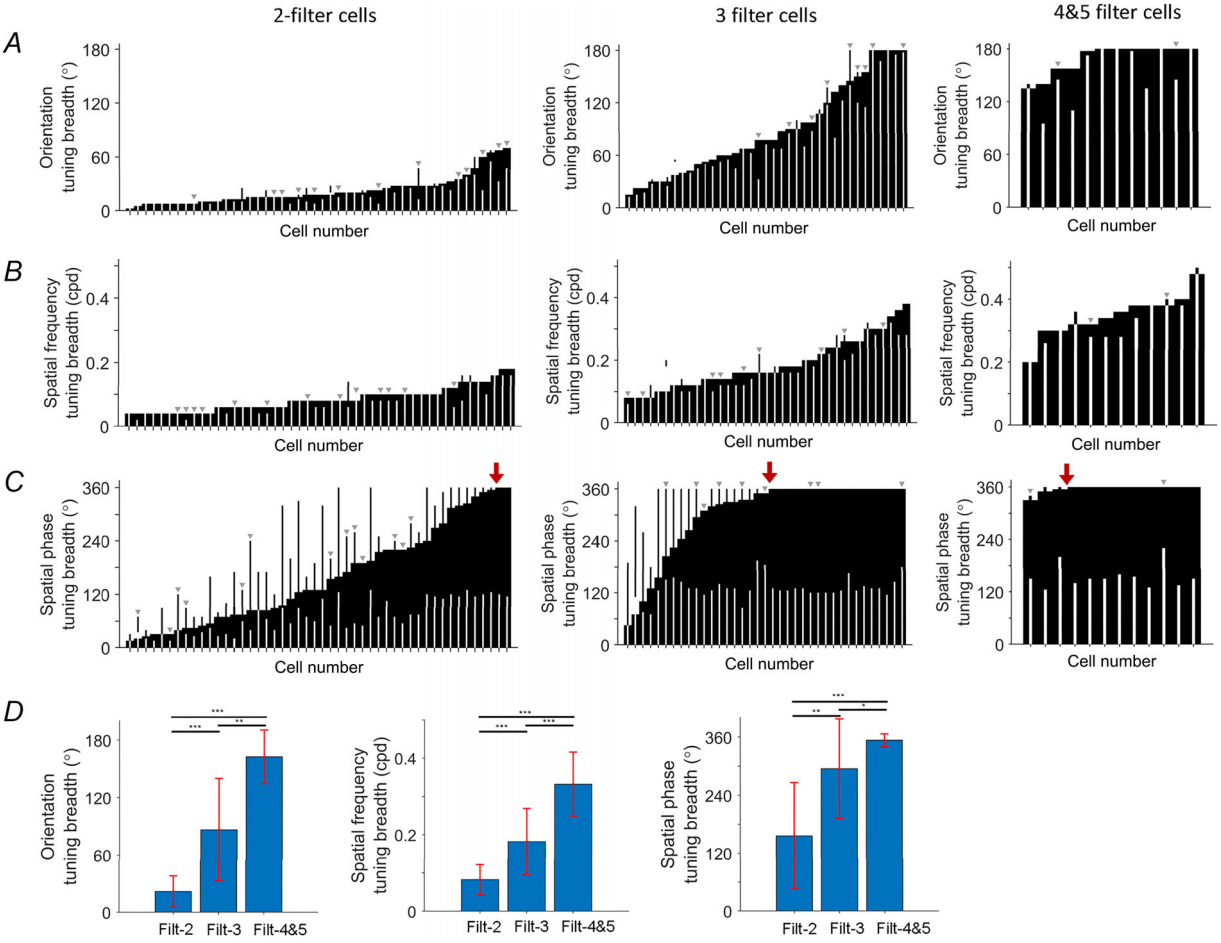

Figure 7. Enhancing feature selectivity or invariance in wallaby V1 cells
Bar graphs illustrate the tuning widths of wallaby V1 cells categorized into three groups: those with two filters (left column), those with three filters (middle column), and those with four and five filters (right column). This analysis is presented across three fundamental feature attributes: (*A*) orientation, (*B*) spatial frequency and (*C*) spatial phase. Each vertical tick mark along the *x*-axis represents an individual cell. The length of each thick black bar corresponds to the tuning width of the respective cell. Occasionally, thin black bars extend beyond the thick bars, indicating the spectral range in feature attributes. The length of the thin white bars represents the width when a linear coding scheme was applied for pooling. Above the bars, light triangular symbols denote cells whose feature spectra contained less than 90% Gabor-like. The red arrows above the bar plots represent when the cell population reaches 360° spatial phase tuning widths. *D*, the average of the spectral range in feature characteristics measured with NIM from cells with filter-2, filter-3 and filter-4 & 5. Orientation tuning breadths (°) for filter-2 (mean ± SD: 21.73 ± 16.42), filter-3 (86.58 ± 53.51), filter-4 & 5 (162.69 ± 27.85). Spatial frequency tuning breadth (cpd) for filter-2 (0.08 ± 0.04), filter-3 (0.18 ± 0.09), filter-4 & 5 (0.33 ± 0.08). Spatial phase tuning breadth (°) for filter-2 (156.12 ± 110.36), filter-3 (294.74 ±102.79), filter-4 & 5 (353.46 ± 13.13). The error bars represent standard deviation. Asterisks represent $^{*}P < 0.05$, $^{**}P < 0.01$, $^{***}P < 0.001$ (*t* test). [Colour figure can be viewed at wileyonlinelibrary.com]

that covered 360° (Fig. 6*C*). For comparison, in cat, 52% of cells with more than three filters had tuning breadths of 360° (Fig. 6*D*), remembering that only 2% of the entire population had more than three filters.

In the broader population of wallaby V1 cells, 57% of multi-filter cells had spatial phase tuning breadths between the upper 360° limit and the lower limit of the linear model. The remaining 43% had breadths at the upper limit, that is complete phase invariance. The 57% of cells with partial spatial phase invariance exceeded what is possible with linear processing, the latter shown by the thin white bars (Fig. 7*C*). For most of these cells, this partial spatial phase invariance was due primarily to their non-linear feature-contrast response functions, which only partly sampled the underlying feature spectrum. Consequently, partial phase invariance was not attributed to the spectral range of spatial phases in the cell's feature spectrum being <360°. It was predominantly cells with just two filters that had limited spectral ranges for spatial phase (Fig. 7*C*).

As shown in Fig. 7*D*, we found that the subpopulation of cells with 3+ filters exhibited greater invariance to larger perturbations in orientation, spatial frequency, and spatial phase than cells with two filters. Specifically, cells with filter-3 (mean ± SD: 86.58 ± 53.51°) and filters-4 & 5 (162.69 ± 27.85°) had significantly larger orientation tuning bandwidths (°) compared to cells with filter-2 (21.73 ± 16.42°), respectively (*t* test: $P > 0.001$, $P > 0.001$). Similarly, cells with filter-3 (0.18 ± 0.09 cpd) and filters-4 & 5 (0.33 ± 0.08 cpd) showed significantly larger spatial frequency tuning bandwidths (cpd) than cells with filter-2 (0.08 ± 0.04), respectively (*t* test: $P > 0.001$, $P > 0.001$). Lastly, cells with filter-3 (294.74 ± 102.79°) and filters-4 & 5 (353.46 ± 13.13°) had significantly greater spatial phase tuning breadth (°) compared to cells with filter-2 (156.12 ± 110.36°), respectively (*t* test: $P > 0.01$, $P > 0.001$).

Interestingly, we observed a significantly greater spectral range in orientation tuning and spatial phase tuning in wallaby V1 cells with more than 2 filters (orientation tuning bandwidth: 105.98 ± 58.55°; spatial phase tuning bandwidth: 309.71 ± 92.34°) compared to cat V1 cells with more than two filters (orientation tuning bandwidth: 72.61 ± 30.12°; spatial phase tuning breadth: 272.52 ± 105.21°) (*t* test: $P > 0.01$, $P > 0.01$). The spectral range of spatial frequency tuning bandwidth was similar for wallaby V1 cells with more than two filters (spatial frequency tuning bandwidth: 0.22 ± 0.11 cpd) and cat V1 cells (spatial frequency tuning bandwidth: 0.28 ± 0.10 cpd) (*t* test: $P = 0.09$).

Comparison to cat V1 cell population

Table 1 lists the percentages of filter types in wallaby cortex and compares it with cat visual cortex (Almasi et al., 2020) ($n = 197$). The number of single filter units is similar between the two species (56% in wallaby *versus* 61% in cat). However, in wallaby V1 45% of multi-filter units have two filters, while it is 77% in cats. Wallabies have 24% of units with three or more filters, while only 9% of units fit into this category in cats. The proportion of units with three or more filters was significantly different between cats and wallabies [χ^2 (1, 392) = 15.36, $P < 0.001$]. While four- and five-filter units are very rare in cat V1 (<2%), they collectively account for 7% of all units in wallaby V1 (Table 1, Fig. 8*A*), which is 16% of the multi-filter units. The quite large population of four- and five-filter units in wallaby V1 highlights a distinct difference from cat V1. In addition, the mean number of filters of the population of multi-filter cells is significantly higher in wallabies than in cats (mean = 2.78 in wallaby; mean = 2.31 in cat, $P < 0.01$) (Fig. 8*B*).

The average SI for multi-filter units in wallaby V1 is higher than in cat V1 (median = 0.68 in wallaby; median = 0.37, $P < 0.01$), revealing a strong bias towards even symmetric functions (quadratic-like characteristics). Interestingly, the average SI for single-filter units in wallaby V1 is positive (median = 0.46), showing a stronger bias towards even symmetric functions than in cat V1. This indicates that many wallaby V1 cells are excited by brightness increments and decrements. In contrast, the average SI for single filter units in cat V1 is negative (median = −0.47), revealing that the polarity of responses to brightness increments and decrements are opposite (linear characteristics).

The average F1/F0 ratios of single filter units are significantly different between the two species (median = 1.09 in wallaby; median = 0.45 in cat, $P < 0.001$) (Fig. 8*D*). The single filter units in wallaby V1, when stimulated with grating stimuli, exhibit more simple-like characteristics than in cats. The average F1/F0 ratios of multi-filter units are similar between the two species (median = 0.58 in wallaby; median = 0.46, $P > 0.1$) (Fig. 8*D*).

We observed weaker orientation bias indices in wallabies than in cats for both single (median = 0.34 in wallaby; median = 0.54 in cat; $P < 0.01$) and multi-filter units (median = 0.33 in wallaby; median = 0.58 in cat; $P < 0.001$) (Fig. 8*E*). The average RF size was marginally larger for wallaby single filter units (median = 3.02°) than for both cat single filter (median = 2.07°, $P < 0.001$) and multi-filter units (median = 2.33°, $P < 0.001$) (Fig. 8*F*).

Laminar organization of V1 cells

We sectioned the brains from which recordings were made and were able to identify six anatomically distinct layers, confirming a previous report (compare Fig. 9*A* with Vidyasagar et al., 1992). Layer 4 has higher cell

densities than other areas, making it stand out as a dense, dark layer in Nissl-stained sections at a depth of ∼1.2–1.5 mm (blue band, Fig. 9). We compared the classification of cells in each layer by assessing the mean F1/F0 ratios (grating stimuli) and the number of spatial filters using NIM. We plot the mean F1/F0 ratios against depth (Fig. 9*B*) in five evenly spaced depth-bins from 0 to 2.5 mm, with 0 being the surface. We found that cells in the upper part (0.5 mm), which consisted primarily of layer 2 cells but with some possibly in layer 1, had high percentages of complex cells, with a mean F1/F0 ratio of 0.6. Layer 4 is found in the 1–1.5 mm depth-bin and

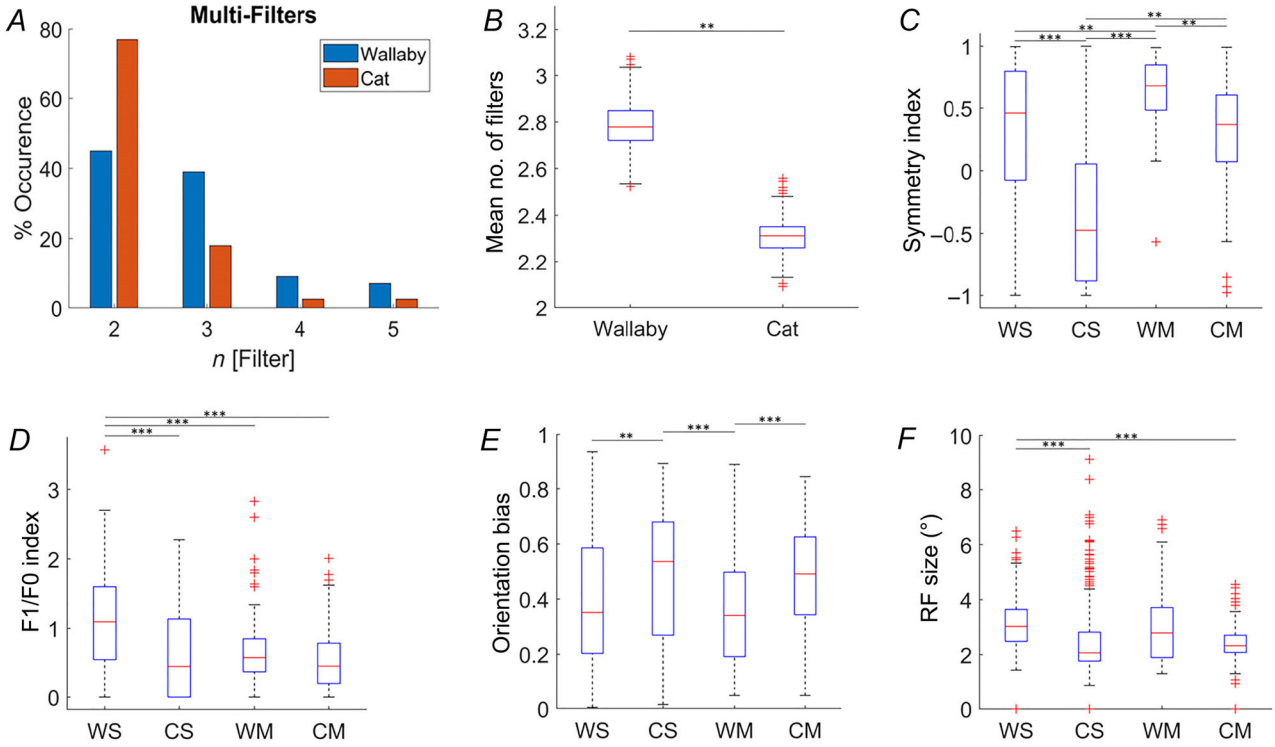

Figure 8. Comparison with cat V1 cells
A, distribution of the number of filters for multi-filter units in wallaby (blue bars) and cat (orange bars). Cat data from Almasi et al. (2020). *B–F*, box plots of (*B*) the mean number of filters, (*C*) symmetry index, (*D*) F1/F0 ratio, (*E*) orientation bias, and (*F*) RF size for wallaby and cat V1 cells. WS = wallaby single-filtered cells, CS = cat single-filtered cells, WM = wallaby multi-filtered cells, CM = cat multi-filtered cells. Asterisks represent $^{*}P < 0.05$, $^{**}P < 0.01$, $^{***}P < 0.001$ (*t* test). [Colour figure can be viewed at wileyonlinelibrary.com]

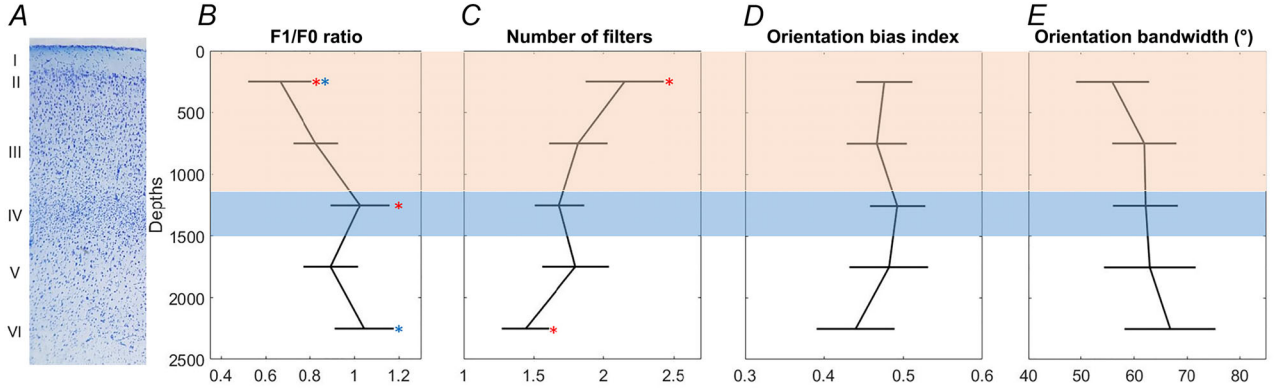

Figure 9. The classification of cells in each layer of the primary visual cortex
A, six anatomically distinct layers shown using Nissl-staining. *B*, mean F1/F0 ratios against depth. *C*, the mean number of filters against depth. *D*, the mean of orientation bias index against depth. *E*, the mean orientation bandwidth against depth. Five evenly spaced depth-bins from 0 to 2.5 mm. [Colour figure can be viewed at wileyonlinelibrary.com]

layer 6 in the 2–2.5 mm depth-bin. The F1/F0 ratios in these depth-bins were significantly higher than for the upper-most depth-bin. Thus, layer 2 (with some putative layer 1) units are dominated by complex RFs, while layers 4 and 6 have significantly higher percentages of simple RFs. We cross-checked these findings using the NIM data and found that the number of filters in the uppermost depth-bin averaged 2.2, which was significantly higher (t test, $P < 0.05$) than the mean number of filters in the lowest depth-bin (1.4) (Fig. 9*C*).

We also wanted to see if non-oriented cells were more common in certain layers. To test for this, we split our cells into orientation selective (OB > 0.2, $n = 148$) and non-oriented (OB < 0.2, $n = 47$) using the OB index. For the non-oriented cells, the mean OB index and mean orientation bandwidths were 0.12 and 138°, respectively, and the cells were evenly distributed between layers. For the cells classed as orientation selective, the mean OBs ranged between 0.35 and 0.6 and showed no significant differences between layers (t test, $P > 0.05$) (Fig. 9*D*). Also, orientation bandwidths did not show significant differences between layers (Fig. 9*E*).

Discussion

Why have more spatial filters?

In a wide range of mammals, the RFs of retinal ganglion cells and neurons in the dorsal lateral geniculate nucleus (dLGN), which conduct the preliminary visual processing prior to V1, have centre-surround RFs that are rarely orientation selective (Devries & Baylor, 1997; Drager, 1975; Hoffmann et al., 1972; Hubel & Wiesel, 1968). Orientation selectivity and segregation into simple and complex cells emerge in V1 (Mechler & Ringach, 2002; Priebe, 2016; Somers et al., 1995). Simple cell RFs can be modelled using one spatial Gabor filter (Chen et al., 2007; Rust et al., 2005). To provide phase invariance, complex cell RFs can be effectively modelled with two spatially offset Gabor filters that form quadrature pairs (Adelson & Bergen 1985; Chen et al., 2007; Emerson et al., 1992; Touryan et al., 2005). In macaque V1, Rust et al. (2005) reported that simple and complex cells with multiple filters exist and recent studies have highlighted a diversity of filters in the cortices of several eutherian mammals, suggesting that both simple and complex cells integrate signals in ways that are not fully accounted for by traditional models (Almasi et al., 2020; Chen et al., 2007; Fournier et al., 2014; Yunzab et al., 2019). Our analysis shows that a particularly diverse range of filter types and numbers exist in marsupial wallaby cortex, compared to eutherian cat (Table 1).

In wallaby V1, 24% of the total number of recorded cells have three or more filters, compared to just 9% in cat. If we only consider multi-filter cells in cat, 77% have just two spatial filters, while this category is only 45% in wallaby cortex. Therefore, for multi-filter cells only 23% in cat have more than two filters, while this percentage in wallabies is far higher (55%). The results show that the information processing in V1 for the two species can be explained well through NIM and that there is clearly a common processing scheme involved. However, we found that wallabies exhibit a statistically higher number of spatial filters than cats for encoding information in V1, perhaps suggesting that wallabies have condensed more capacity to build phase invariance into the first step in the cortical pathway. Similar evidence of condensed early processing has been shown in rodent V1, where a large fraction of cells is sensitive to the pattern motion direction of a plaid, rather than the directions of the plaid's component edges (De Vries et al., 2020; Palagina et al., 2017). In total, 74% of neurons in the mouse visual cortex have orientation selectivity (Neil & Stryker, 2008), which is comparable to 76% reported in the wallaby V1. Sharper tuning was observed in layer 2/3 than in other layers for mouse, whereas in the wallaby, there was no significant laminar difference. In total, 22% of cells in the mouse visual cortex were classified as complex-like with multiple filters based on the linear–non-linear models (Ukita et al. 2019), whereas 44% of cells in the wallaby visual cortex are found to be complex-like with multiple filters based on our analysis. So, the complex-like features are much greater in the wallaby than in the mouse.

For comparison, in primates, the processing of pattern direction with plaids is far more common in higher-order visual areas, starting in Area V5 (MT) (Wang & Movshon, 2016).

Theoretically, just a single quadrature pair of ideal Gabor filters should be able to give 360° phase invariance (Adelson & Bergen 1985). However, in practice, we have found that few two-filter cells in cat and wallaby are truly phase invariant and that most non-linear functions are not perfectly even symmetric. Almasi et al. (2020) assessed the advantages offered by adding more filters in cat V1 but absolute cell numbers were low, making a population analysis problematic. They found that there was greater feature invariance (i.e. spatial phase, orientation and spatial frequency) for cells with three or more filters compared to those with just two filters. In the wallaby, we have the advantage that 24% of all cells have three or more filters, allowing a meaningful population analysis. This analysis reveals that the great majority have spatial phase breadths close to the maximum value of 360°. Moreover, the tuning breadths for orientation are far wider across this subpopulation of cells than in cells with two or fewer filters. Our findings reveal that both species have the capacity to increase invariance by adding filters, but that wallaby V1 has greatly emphasized this characteristic in its cell population. In higher-order cat visual areas (i.e. Areas 19 and 21a) we find high percentages of cells with three or

more filters (our unpublished observations), reinforcing the idea that wallaby cortex condenses more processing into earlier steps, while cats distribute the processing across more areas.

Almasi et al. (2020) showed that the few cells in cat V1 with three or more filters also had a high proportion of filters (32%) with mixed blob-like and Gabor-like characteristics. In wallaby V1 we observe the same phenomena, but the wallaby has a far higher percentage of these cell types. In our wallaby analysis, we found that when responses were measured using drifting gratings, even the cells with some blob-like filters are orientation selective. We suggest that by combining multiple blob-like filters in these cells, some additional processing capacity that is not yet fully understood may be offered; for example, they may enhance a cell's ability to respond to an oriented edge embedded in texture. Interestingly, Goris et al. (2015) used a parametric cascade model with one orientation selective filter (i.e. Gabor-like) and one non-oriented filter (i.e. blob-like). They showed that orientation and spatial frequency tuning in macaque V1 can be extracted with this model. In their scheme, the excitatory contribution of the blob-like filters generates a broadening of the overall orientation tuning. We also found that the orientation and spatial frequency tuning of V1 cells was determined largely by the spectrum of filters, with the non-linearity having little impact (Almasi et al., 2020; Yunzab et al., 2019).

Non-linear properties of V1 units

In cat V1, Almasi et al. (2020) showed that invariance to spatial phase depends primarily on the non-linear input function. In wallaby, the input function for each filter was characterized by a symmetry index. Traditionally, simple cells are modelled as having a single Gabor spatial filter with a monotonically increasing input function with opposite responses to opposite feature-contrasts (odd symmetric). Conversely, complex cells are modelled with two Gabor filters that form a quadrature pair (Chen et al., 2007; Rust et al., 2005; Touryan et al., 2002, 2005). In this case the input functions would respond equally to opposing feature-contrasts and have an even symmetric characteristic.

In contrast to these expectations, recent studies (Almasi et al., 2020; Chen et al., 2007; Jung et al., 2022; Touryan et al., 2005) have found that a large percentage of single-filter cells show non-linear properties; for example, 40% of classically defined complex cells in cat V1 have a single filter. In wallaby, we found that almost 30% of single-filter cells exhibited even-symmetric input functions, and that close to 86% of single-filter cells were classified as complex cells when using F1/F0 ratios (for the perils of using F1/F0 ratios, see Hietanen et al. 2013). Cat retina and dLGN have both X- and Y-cells (Golstein et al., 2015; Goris et al., 2015; Hietanen et al., 2013). X-cells have linear summation properties while Y-cells have very non-linear summation, the latter revealed by their spiking responses to both ON-and-OFF stimulation (Enroth-Cugell & Robson, 1966). The existence of single-filter units in wallabies with either linear or non-linear summation is probably linked to their connectivity with the dLGN. In support of this idea, recordings from wallaby dLGN revealed cells with X-like and Y-like characteristics (Henry & Mark 1992). In cats, more single filter cells show complex-like features (F1/F0 ratio < 1, 40%) exhibiting non-linearities that reduce the response at the fundamental frequency (Almasi et al., 2020). This could be because cats have more Y cells in the primary visual cortex showing non-linear summation than in wallabies. The F1/F0 ratio does not provide any information on the RF geometry (e.g. number and shape of subregions), so cells with single filter RF can be classified as complex-like based on the non-linear summation of responses.

For V1 units with multiple filters, input functions were most frequently quadratic-like, but most were not perfectly even-symmetric, and others were not similar to quadratics. We found a greater diversity in feature-contrast response functions than predicted by traditional models, such as the energy model (Adelson & Bergen, 1985; Emerson et al., 1992) as also reported for complex RF filters in cat (Almasi et al., 2020; Touryan et al., 2005).

Non-orientation selective units

Early analysis of orientation selectivity in marsupial cortex, which generally used hand-plotting techniques, revealed relatively low proportions of orientation selectivity (∼30–50%) (American opossum: Rocha-Miranda et al. 1976; Australian brush-tailed possum: Crewther et al. 1984). An analysis of wallaby cortex using drifting gratings revealed that 70% of cells were orientation selective (Ibbotson et al., 2003). Here, using an objective analysis of responses to WGN, we found a similar value: 76% of cells were orientation selective. Therefore, approximately a quarter of wallaby V1 cells are non-orientation selective, a value that is similar to modern population analyses of cat cortex based on recordings using multi-electrode arrays (Gharat & Baker, 2017; Sun et al., 2021).

The non-orientation selective RFs in wallaby V1 have almost circular central regions that respond to ON, OFF or ON–OFF stimulation (e.g. Fig. 3, cell #1). No obvious surround-antagonism was observed; for example, if the centre was ON, we did not see a robust OFF surround, or vice versa. Centre-surround antagonism is a common feature of cells in retina, dLGN and some V1 cells, when stimulated with high-contrast stimuli

(Gharat & Baker, 2017; Ruksenas et al., 2000; Sun et al., 2021). Henry and Mark (1992) reported ON, OFF and ON–OFF sensitive units in wallaby dLGN, with an over-representation of ON and a marked under-representation of ON–OFF sensitivity. They did not quantify the surround antagonism. The lack of surround antagonism in our data may be due to the use of WGN stimuli. One of the functional roles of centre-surround RFs is to 'whiten' natural images, i.e. reduce response amplitudes to low spatial frequencies and enhance responses to high spatial frequencies, thus overcoming the bias towards low spatial frequencies in natural scenes (Doi et al., 2003; Graham et al., 2006). As our stimulus consisted of noise that was already spatially white, it may have not engaged the whitening mechanism of the visual system. A similar lack of apparent surround suppression was noted in non-oriented units in cat cortex (Almasi et al., 2020; Sun et al., 2021).

Suppressive filters

In wallaby, we found filters with purely excitatory and mixed excitatory–suppressive filters, but no units with purely suppressive filters. The NIM was able to identify units with mixed excitatory–suppressive filters because we had identified input functions with suppressive effects during RF estimation. The lack of pure inhibitory filters was consistent with several studies that have conducted extracellular recordings in cat V1 (Almasi et al., 2020; Simoncelli et al., 2004; Touryan et al., 2002). Other studies have found purely suppressive filters in RFs from intracellular recordings in cat V1 (Fournier et al., 2014) and monkey V1 (Chen et al., 2007; Rust et al., 2005). The lack of suppressive filters might be linked to the relatively low numbers of recorded spikes in cat and wallaby V1, interspecies differences or the effects of differing anaesthetics (Chen et al., 2007; De Vries et al., 2020; Touryan et al., 2005).

Laminar organization of V1 cells

In general, across mammals, cortical layer 4 receives the main inputs from the dLGN (Douglas & Martin, 2004), and inputs may also innervate a thin stratum at the top of layer 6 (Briggs & Usrey, 2007). Layer 1 is a sparse layer filled mainly with axons arising from multiple cortical and subcortical areas that innervate the apical dendrites of cortical pyramidal cells. Layers 2 and 3 receive their primary inputs from layer 4 cells and send information to other cortical regions (Yabuta & Callaway, 1998). Layers 5 and 6 get inputs from layers 2–4 and send their axons into the superior colliculus and dLGN, respectively (May, 2006). In some species, layer 4 has a higher proportion of non-orientation selective cells, in accordance with the direct inputs from dLGN, which tend to be non-orientation selective (e.g. tree shrew: Bosking et al., 1997). We did not find any predominance of non-oriented cells in wallaby layer 4. In fact, the non-oriented cells were dispersed quite evenly throughout the cortical layers, but always in small proportions compared to oriented cells.

Our laminar analysis revealed that cells with larger numbers of spatial filters were located in the uppermost strata, most being cells in layer 2. Cells with more filters offer a higher level of image processing and so it is logical that these cell types would be found in strata feeding higher cortical areas. Conversely, the strata with the highest numbers of simple cells (defined using F1/F0 analysis) and the lowest mean number of spatial filters (defined using NIM) corresponded with layers 4 and 6. In primates, layer 4 tends to have a higher proportion of simple cells, suggesting that this cell type forms an early stage in cortical processing, only one synapse removed from the dLGN inputs (Cloherty et al. 2015; Ringach et al. 2002; Wang et al. 2020). Our observations from wallaby cortex are in accordance with the observations made in primate cortex, suggesting that marsupial cortex has evolved along similar lines, despite a total segregation from the Eutherian line for 160 million years. This incredible level of conservation or convergent evolution of high-level visual processing across diverse species and visual environments is a very significant observation.

References

Adelson, E. H., & Bergen, J. R. (1985). Spatiotemporal energy models for the perception of motion. *Journal of the Optical Society of America A, Optics and Image Science*, **2**(2), 284–99.

Almasi, A., Meffin, H., Cloherty, S. L., Wong, Y., Yunzab, M., & Ibbotson, M. R. (2020). Mechanisms of feature selectivity and invariance in primary visual cortex. *Cerebral Cortex*, **30**(9), 5067–5087.

Almasi, A., Sun, S. H., Yunzab, M., Jung, Y. J., Meffin, H., & Ibbotson, M. R. (2022). How stimulus statistics affect the receptive fields of cells in primary visual cortex. *Journal of Neurosciencie*, **42**(26), 5198–5211.

Azevedo, F. A., Carvalho, L. R., Grinberg, L. T., Farfel, J. M., Ferretti, R. E., Leite, R. E., Filho, W. J., Lent, R., & Herculano-Houzel, S. (2009). Equal numbers of neuronal and nonneuronal cells make the human brain an isometrically scaled-up primate brain. *Journal of Comparative Neurology*, **513**(5), 532–541.

Bosking, W. H., Zhang, Y., Schofield, B., & Fitzpatrick, D. (1997). Orientation selectivity and the arrangement of horizontal connections in tree shrew striate cortex. *Journal of Neuroscience*, **17**(6), 2112–2127.

Briggs, F., & Usrey, W. M. (2007). A fast, reciprocal pathway between the lateral geniculate nucleus and visual cortex in the macaque monkey. *Journal of Neuroscience*, **27**(20), 5431–5436.

Chen, X., Han, F., Poo, M. M., & Dan, Y. (2007). Excitatory and suppressive receptive field subunits in awake monkey primary visual cortex (V1). *Proceedings of the National Academy of Sciences*, **104**(48), 19120–19125.

Cloherty, S. L., & Ibbotson, M. R. (2015). Contrast-dependent phase sensitivity in V1 but not V2 of macaque visual cortex. *Journal of Neurophysiology*, **113**(2), 434–444.

Crewther, D. P., Crewther, S. G., & Sanderson, K. J. (1984). Primary visual cortex in the brushtailed possum: receptive field properties and corticocortical connections. *Brain, Behavior and Evolution*, **24**(4), 184–197.

Crowder, N. A., Hietanen, M. A., Price, N. S., Clifford, C. W., & Ibbotson, M. R. (2008). Dynamic contrast change produces rapid gain control in visual cortex. *The Journal of Physiology*, **586**(17), 4107–4119.

De Vries, S. E., Lecoq, J. A., Buice, M. A., Groblewski, P. A., Ocker, G. K., Oliver, M., Feng, D., Cain, N., Ledochowitsch, P., Millman, D., & Roll, K. (2020). A large-scale standardized physiological survey reveals functional organization of the mouse visual cortex. *Nature Neuroscience*, **23**(1), 138–151.

Devries, S. H., & Baylor, D. A. (1997). Mosaic arrangement of ganglion cell receptive fields in rabbit retina. *Journal of Neurophysiology*, **78**(4), 2048–2060.

Doi, E., Inui, T., Lee, T. W., Wachtler, T., & Sejnowski, T. J. (2003). Spatiochromatic receptive field properties derived from information-theoretic analyses of cone mosaic responses to natural scenes. *Neural Computation*, **15**(2), 397–417.

Douglas, R. J., & Martin, K. A. (2004). Neuronal circuits of the neocortex. *Annual Review of Neuroscience*, **27**(1), 419–451.

Dräger, U. C. (1975). Receptive fields of single cells and topography in mouse visual cortex. *Journal of Comparative Neurology*, **160**(3), 269–289.

Emerson, R. C., Bergen, J. R., & Adelson, E. H. (1992). Directionally selective complex cells and the computation of motion energy in cat visual cortex. *Vision Research*, **32**(2), 203–218.

Enroth-Cugell, C., & Robson, J. G. (1966). The contrast sensitivity of retinal ganglion cells of the cat. *The Journal of Physiology*, **187**(3), 517–552.

Felleman, D. J., & Van Essen, D. C. (1991). Distributed hierarchical processing in the primate cerebral cortex. *Cerebral Cortex (New York, NY: 1991)*, **1**(1), 1–47.

Fournier, J., Monier, C., Levy, M., Marre, O., Sári, K., Kisvárday, Z. F., & Frégnac, Y. (2014). Hidden complexity of synaptic receptive fields in cat V1. *Journal of Neuroscience*, **34**(16), 5515–5528.

Gharat, A., & Baker, C. L. (2017). Nonlinear Y-like receptive fields in the early visual cortex: An intermediate stage for building cue-invariant receptive fields from subcortical Y cells. *Journal of Neuroscience*, **37**(4), 998–1013.

Goltstein, P. M., Montijn, J. S., & Pennartz, C. M. (2015). Effects of isoflurane anesthesia on ensemble patterns of Ca^{2+} activity in mouse v1: Reduced direction selectivity independent of increased correlations in cellular activity. *PLoS ONE*, **10**(2), e0118277.

Goris, R. L., Simoncelli, E. P., & Movshon, J. A. (2015). Origin and function of tuning diversity in macaque visual cortex. *Neuron*, **88**(4), 819–831.

Graham, D. J., Chandler, D. M., & Field, D. J. (2006). Can the theory of "whitening" explain the center-surround properties of retinal ganglion cell receptive fields?. *Vision Research*, **46**(18), 2901–2913.

Henry, G. H., & Mark, R. F. (1992). Partition of function in the morphological subdivisions of the lateral geniculate nucleus of the tammar wallaby (*Macropus eugenii*). *Brain Behavior and Evolution*, **39**(6), 358–370.

Hietanen, M. A., Cloherty, S. L., Van Kleef, J. P., Wang, C., Dreher, B., & Ibbotson, M. R. (2013). Phase sensitivity of complex cells in primary visual cortex. *Neuroscience*, **237**, 19–28.

Hoffmann, K. P., Stone, J., & Sherman, S. M. (1972). Relay of receptive-field properties in dorsal lateral geniculate nucleus of the cat. *Journal of Neurophysiology*, **35**(4), 518–531.

Hubel, D. H., & Wiesel, T. N. (1959). Receptive fields of single neurones in the cat's striate cortex. *The Journal of Physiology*, **148**(3), 574.

Hubel, D. H., & Wiesel, T. N. (1962). Receptive fields, binocular interaction and functional architecture in the cat's visual cortex. *The Journal of Physiology*, **160**(1), 106.

Hubel, D. H., & Wiesel, T. N. (1968). Receptive fields and functional architecture of monkey striate cortex. *The Journal of Physiology*, **195**(1), 215–243.

Ibbotson, M. R., & Mark, R. F. (2003). Orientation and spatiotemporal tuning of cells in the primary visual cortex of an Australian marsupial, the wallaby Macropus eugenii. *Journal of Comparative Physiology*, **189**(2), 115–123.

Ibbotson, M. R., Price, N. S., & Crowder, N. A. (2005). On the division of cortical cells into simple and complex types: a comparative viewpoint. *Journal of Neurophysiology*, **93**(6), 3699–3702.

Inan, M., & Crair, M. C. (2007). Development of cortical maps: perspectives from the barrel cortex. *The Neuroscientist*, **13**(1), 49–61.

Jung, Y. J., Almasi, A., Sun, S. H., Yunzab, M., Cloherty, S. L., Bauquier, S. H., Renfree, M., Meffin, H., & Ibbotson, M. R. (2022). Orientation pinwheels in primary visual cortex of a highly visual marsupial. *Science Advances*, **8**(39), eabn0954.

Jung, Y. J., Sun S. H., Almasi A., Yunzab M., Meffin H., & Ibbotson M. R. (2023). Characterization of extracellular spike waveforms recorded in wallaby primary visual cortex. *Frontiers in Neuroscience*, **17**, 1244952.

Kendrick, K. M., Atkins, K., Hinton, M. R., Heavens, P., & Keverne, B. (1996). Are faces special for sheep? Evidence from facial and object discrimination learning tests showing effects of inversion and social familiarity. *Behavioural Processes*, **38**(1), 19–35.

Kravitz, D. J., Saleem, K. S., Baker, C. I., Ungerleider, L. G., & Mishkin, M. (2013). The ventral visual pathway: an expanded neural framework for the processing of object quality. *Trends in Cognitive Sciences*, **17**(1), 26–49.

Liu, L., She, L., Chen, M., Liu, T., Lu, H. D., Dan, Y., & Poo, M. M. (2016). Spatial structure of neuronal receptive field in awake monkey secondary visual cortex (V2). *Proceedings of the National Academy of Sciences*, **113**(7), 1913–1918.

Luo, Z., Yuan, X., Meng, J., & Ji, Q. (2011). A Jurassic eutherian mammal and divergence of marsupials and placentals. *Nature*, **476**(7361), 442–445.

May, P. J. (2006). The mammalian superior colliculus: laminar structure and connections. *Progress in Brain Research*, **151**, 321–378.
McFarland, J. M., Cui, Y., & Butts, D. A. (2013). Inferring nonlinear neuronal computation based on physiologically plausible inputs. *PLoS Computational Biology*, **9**(7), e1003143.
Mechler, F., & Ringach, D. L. (2002). On the classification of simple and complex cells. *Vision Research*, **42**(8), 1017–1033.
Niell, C. M., & Stryker, M. P. (2008). Highly selective receptive fields in mouse visual cortex. *Journal of Neuroscience*, **28**(30), 7520–7536.
Nishimoto, S., Ishida, T., & Ohzawa, I. (2006). Receptive field properties of neurons in the early visual cortex revealed by local spectral reverse correlation. *Journal of Neuroscience*, **26**(12), 3269–3280.
Pachitariu, M., Steinmetz, N. A., Kadir, S. N., Carandini, M., & Harris, K. D. (2016). Fast and accurate spike sorting of high-channel count probes with KiloSort. *Advances in Neural Information Processing Systems*, **29**.
Palagina, G., Meyer, J. F., & Smirnakis, S. M. (2017). Complex visual motion representation in mouse area V1. *Journal of Neuroscience*, **37**(1), 164–183.
Priebe, N. J. (2016). Mechanisms of orientation selectivity in the primary visual cortex. *Annual Review of Vision Science*, **2**(1), 85–107.
Riesenhuber, M., & Poggio, T. (1999). Hierarchical models of object recognition in cortex. *Nature Neuroscience*, **2**(11), 1019–1025.
Ringach, D. L., Shapley, R. M., & Hawken, M. J. (2002). Orientation selectivity in macaque V1: Diversity and laminar dependence. *Journal of Neuroscience*, **22**(13), 5639–5651.
Rocha-Miranda, C. E., Linden, R., Volchan, E., Lent, R., & Bombardieri, R. A. Jr. (1976). Receptive field properties of single units in the opossum striate cortex. *Brain Research*, **104**(2), 197–219.
Rossant, C., Kadir, S. N., Goodman, D. F., Schulman, J., Hunter, M. L., Saleem, A. B., Grosmark, A., Belluscio, M., Denfield, G. H., Ecker, A. S., & Tolias, A. S. (2016). Spike sorting for large, dense electrode arrays. *Nature Neuroscience*, **19**(4), 634–641.
Ruksenas, O., Fjeld, I. T., & Heggelund, P. (2000). Spatial summation and center-surround antagonism in the receptive field of single units in the dorsal lateral geniculate nucleus of cat: comparison with retinal input. *Visual Neuroscience*, **17**(6), 855–870.
Rust, N. C., Schwartz, O., Movshon, J. A., & Simoncelli, E. P. (2005). Spatiotemporal elements of macaque v1 receptive fields. *Neuron*, **46**(6), 945–956.
Sharpee, T. O., Sugihara, H., Kurgansky, A. V., Rebrik, S. P., Stryker, M. P., & Miller, K. D. (2006). Adaptive filtering enhances information transmission in visual cortex. *Nature*, **439**(7079), 936–942.
Simoncelli, E. P., Paninski, L., Pillow, J., & Schwartz, O. (2004). Characterization of neural responses with stochastic stimuli. *The Cognitive Neurosciences*, **3**, 327–338
Skottun, B. C., De Valois, R. L., Grosof, D. H., Movshon, J. A., Albrecht, D. G., & Bonds, A. B. (1991). Classifying simple and complex cells on the basis of response modulation. *Vision Research*, **31**(7–8), 1078–1086.
Somers, D. C., Nelson, S. B., & Sur, M. (1995). An emergent model of orientation selectivity in cat visual cortical simple cells. *Journal of Neuroscience*, **15**(8), 5448–5465.
Sun, S. H., Almasi, A., Yunzab, M., Zehra, S., Hicks, D. G., Kameneva, T., Ibbotson, M. R., & Meffin, H. (2021). Analysis of extracellular spike waveforms and associated receptive fields of neurons in cat primary visual cortex. *The Journal of Physiology*, **599**(8), 2211–2238.
Touryan, J., Felsen, G., & Dan, Y. (2005). Spatial structure of complex cell receptive fields measured with natural images. *Neuron*, **45**(5), 781–791.
Touryan, J., Lau, B., & Dan, Y. (2002). Isolation of relevant visual features from random stimuli for cortical complex cells. *Journal of Neuroscience*, **22**(24), 10811–10818.
Ukita, J., Yoshida, T, & Ohki, K. (2019). Characterisation of nonlinear receptive fields of visual neurons by convolutional neural network. *Scientific Reports*, **9**(1), 3791–3799.
Vidyasagar, T. R., Wye-Dvorak, J., Henry, G. H., & Mark, R. F. (1992). Cytoarchitecture and visual field representation in area 17 of the tammar wallaby (Macropus eugenii). *Journal of Comparative Neurology*, **325**(2), 291–300.
Wang, H. X., & Movshon, J. A. (2016). Properties of pattern and component direction-selective cells in area MT of the macaque. *Journal of Neurophysiology*, **115**(6), 2705–2720.
Wimborne, B., Mark, R., & Ibbotson, M. (1999). Distribution of retinogeniculate cells in the tammar wallaby in relation to decussation at the optic chiasm. *Journal of Comparative Neurology*, **405**(1), 128–140.
Wang, T., Li, Y., Yang, G., Dai, W., Yang, Y., Han, C., Wang, X., Zhang, Y., & Xing, D. (2020). Laminar subnetworks of response suppression in macaque primary visual cortex. *Journal of Neuroscience*, **40**(39), 7436–7450.
Yabuta, N. H., & Callaway, E. M. (1998). Functional streams and local connections of layer 4C neurons in primary visual cortex of the macaque monkey. *Journal of Neuroscience*, **18**(22), 9489–9499.
Yunzab, M., Cloherty, S. L., & Ibbotson, M. R. (2019). Comparison of contrast-dependent phase sensitivity in primary visual cortex of mouse, cat and macaque. *Neuroreport*, **30**(14), 960.

Additional information

Data availability statement

All data needed to evaluate the conclusions in the paper are present in the paper. The data used to generate these results have been deposited and are available through https://figshare.com/s/5ea253959747db72e118 (cell data).

Competing interests

The authors declare that the research was conducted in the absence of any commercial or financial relationships that could be construed as a potential conflict of interest.

Author contributions

M.I. and Y.J.: conceptualization and writing (original draft). Y.J., S.S., A.A., H.M. and M.I.: methodology. Y.J., A.A., S.S., M.Y., H.M. and M.I.: investigation. Y.J. and S.S.: visualization. M.I.: funding acquisition. M.I. and H.M.: supervision. M.I., Y.J., A.A., S.S., M.Y. and H.M.: writing (review and editing). All authors contributed to the article and approved the submitted version.

Funding

Australian Research Council Centre of Excellence for Integrative Brain Function: Young Jun Jung, CE140100007; Australian Research Council Centre of Excellence for Integrative Brain Function: Michael Ibbotson, CE140100007.

Acknowledgements

This work was supported by the Australian Research Council Centre of Excellence for Integrative Brain Function (Grant CE140100007).

Authors' present addresses

A. Almasi: Optalert Limited, Melbourne, VIC, Australia. S. Sun and M. Yunzab: Department of Neurosurgery, Massachusetts General Hospital, Harvard Medical School, Boston, MA 02114, USA.

Keywords

brain evolution, marsupial, neuroscience, receptive field, visual cortex

Supporting information

Additional supporting information can be found online in the Supporting Information section at the end of the HTML view of the article. Supporting information files available:

Peer Review History